Technical Aspects of GEp-III/GEp-2γ Final Analysis

Andrew Puckett
University of Connecticut

Hall C Collaboration Meeting

January 23, 2018

Outline

- Introduction/overview of final analysis of experiments E04-108 (GEp-III)/E04-019 (GEp-2γ)
- New HMS optics calibrations: angle and vertex reconstruction
- Hall C FPP performance, alignment, and polarimetry
- HMS spin transport systematics
  - Non-dispersive-plane optics/quadrupole misalignment study
- Final evaluation of GEp-III/GEp-2γ systematics

Acknowledgements

- GEp-III spokespeople and core collaborators:
  - Charles Perdrisat, Vina Punjabi, Ed Brash, Mark Jones, Lubomir Pentchev, Frank Wesselmann
- Fellow GEp grad students:
  - Mehdi Meziane
  - Wei Luo
- GEp-III collaboration
- Hall C and JLab Technical Staff
- Support from US DOE, Office of Science, Office of Nuclear Physics, Award ID DE-SC0014230 (Early Career research program)

The GEp-III and GEp-2γ experiments in Hall C

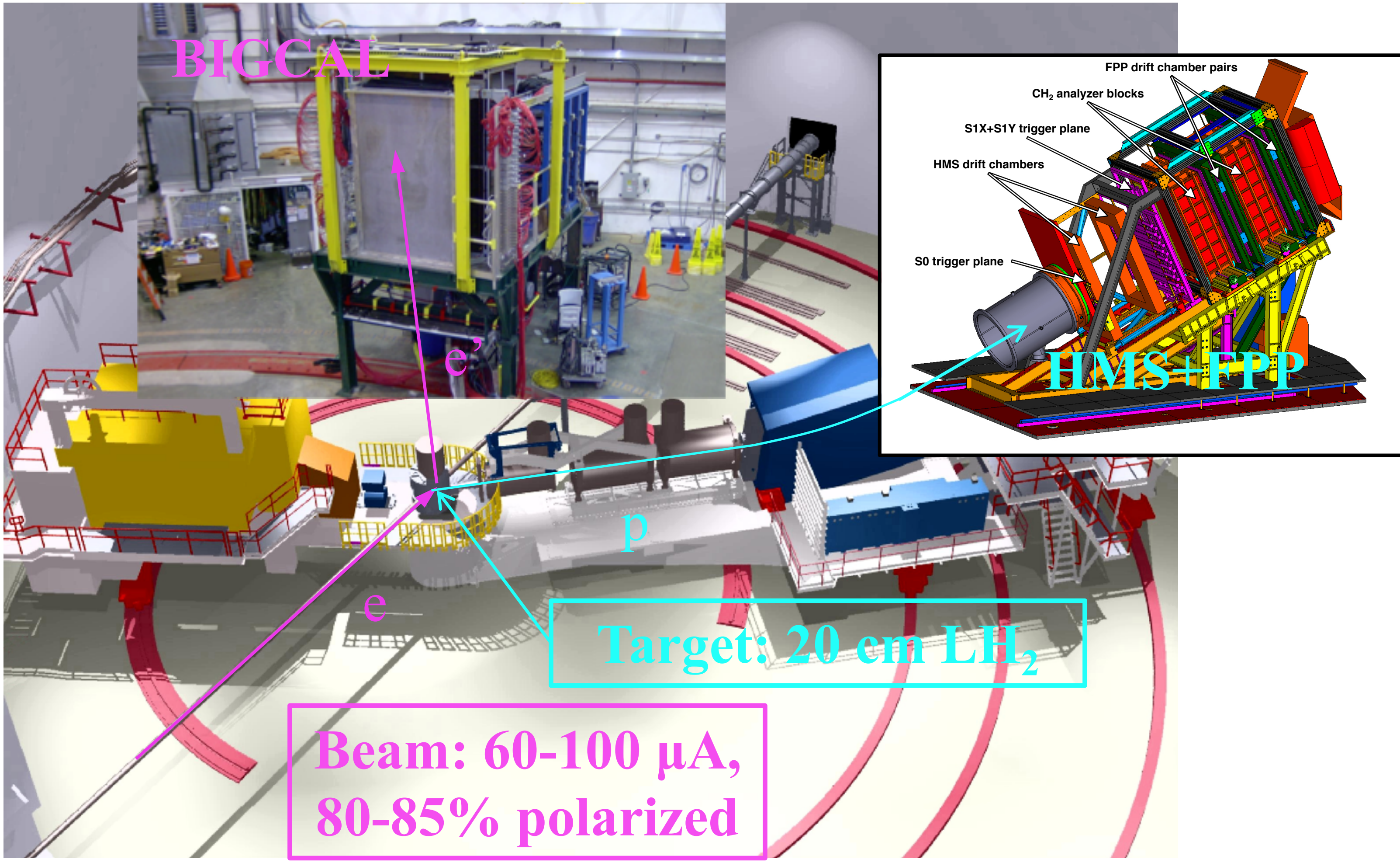

- Polarization transfer in ^{1}H(**e**,e'**p**). Nominal luminosity ~ 4×10^{38} Hz/cm^2
- "Fast" beam helicity reversal (30 Hz) cancels FPP instrumental asymmetry in polarization transfer observables

GEp-III/GEp-2γ Final Results: Phys. Rev. C 96, 055203 (2017)

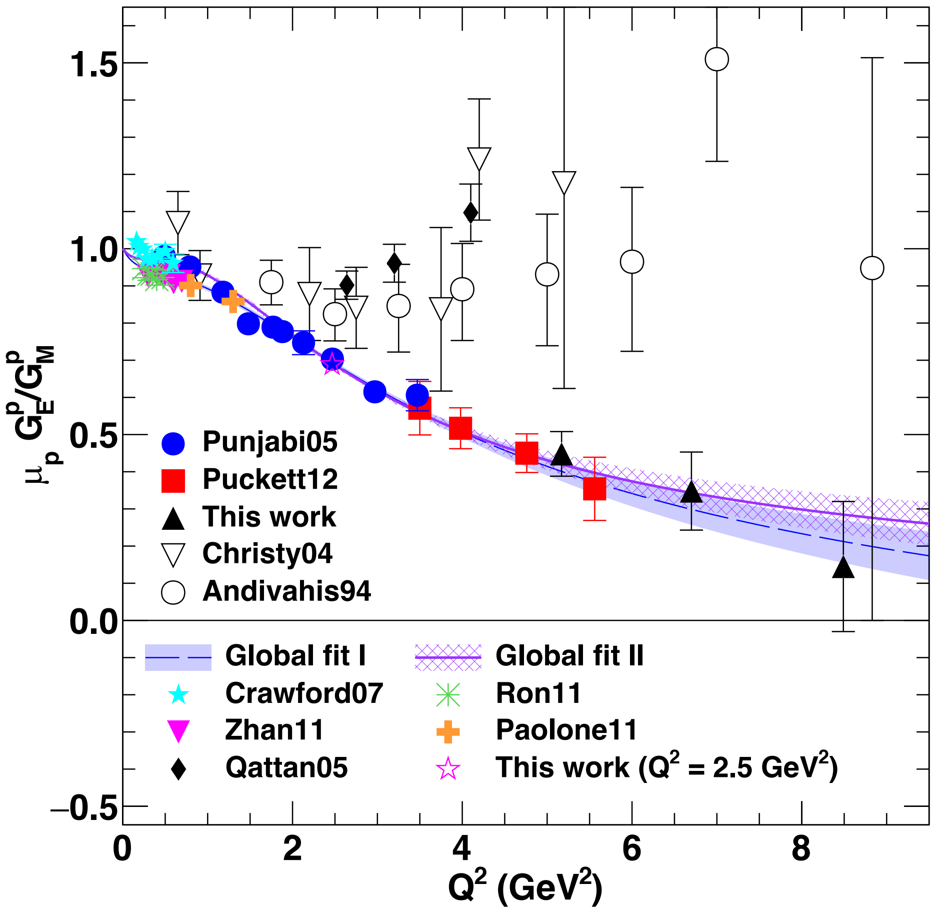

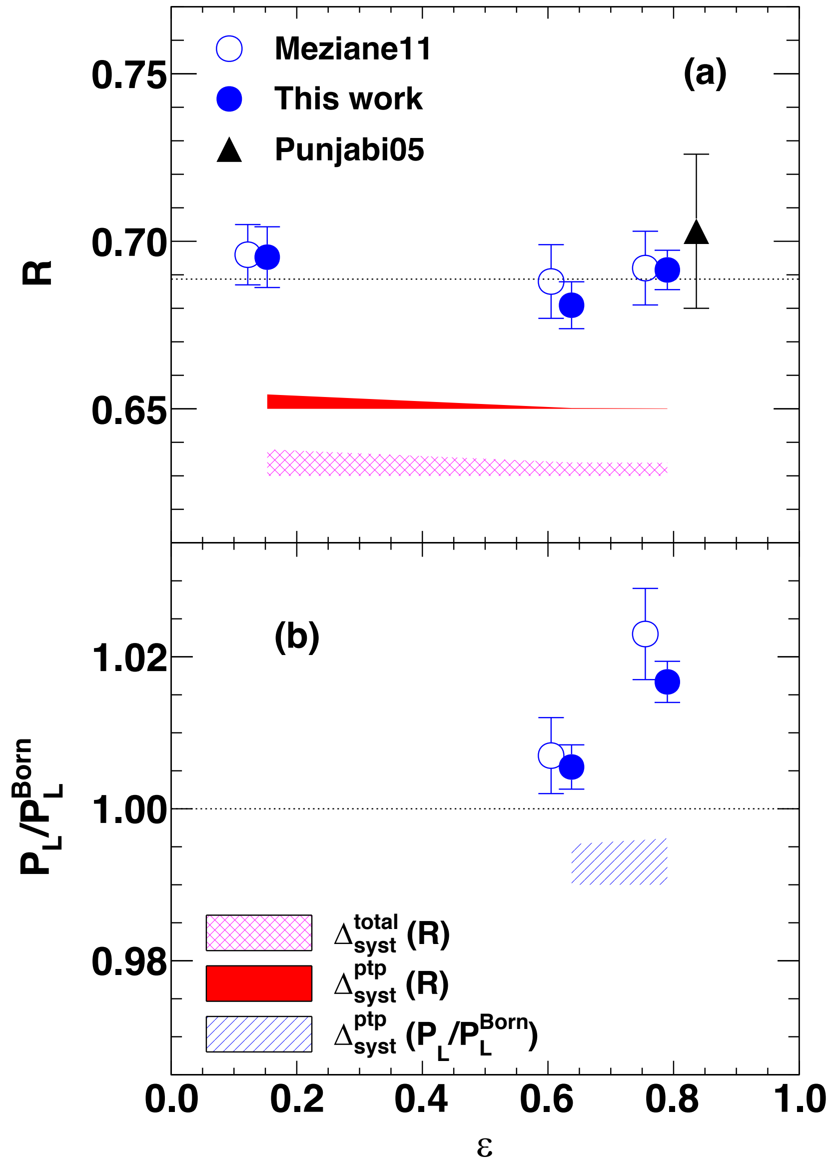

See JLab Physics Seminar, this Friday, Jan. 26, CEBAF Center Auditorium

Overview of new/final analysis of the Hall C data

- Goal: Improve understanding of systematic uncertainties in order to publish full-acceptance results from GEp-2γ and final archival results from GEp-2γ and GEp-III.
- Major aspects of event reconstruction/calibration revisited:
  - **HMS optics calibration: improved angle and vertex reconstruction, well-behaved in a wider phase space**
  - **HMS and FPP time-to-distance calibration performed run-by-run (and card-by-card for FPP drift chambers)**
  - **Improved FPP-HMS drift chamber alignment from straight-through data**
  - Minor improvements/bug fixes to HMS/FPP tracking algorithms
  - Recalibration of BigCal energy reconstruction for some run ranges
  - Minor improvements to BigCal shower coordinate reconstruction
  - Updated beam position/energy database from EPICS (beam position + raster corrections important for momentum/out-of-plane angle reconstruction)
  - More thorough run-by-run data quality checks
    - Exclusion of runs with significant FPP data quality issues from GEp-2gamma analysis (minimize false asymmetries)
    - Fix minor problems with beam polarization database
- Major aspects of physics analysis revisited:
  - Use of more efficient variable-width exclusivity cuts to account for variations of the widths of several exclusivity cut variables within the HMS acceptance (compared to fixed-width cuts used in the analysis for PRL publications)
  - Improved "fully differential" description of the analyzing power for $Q^2 = 2.5$ GeV^2
  - Accounting for finite-acceptance/bin-centering effects on P_T, P_L, R
  - More thorough analysis of the non-dispersive-plane optical study of the HMS to reduce systematic uncertainties due to spin precession calculation.
  - Final evaluation of systematic uncertainties

HMS Optics Calibration—Sieve Slit/Vertex Reconstruction

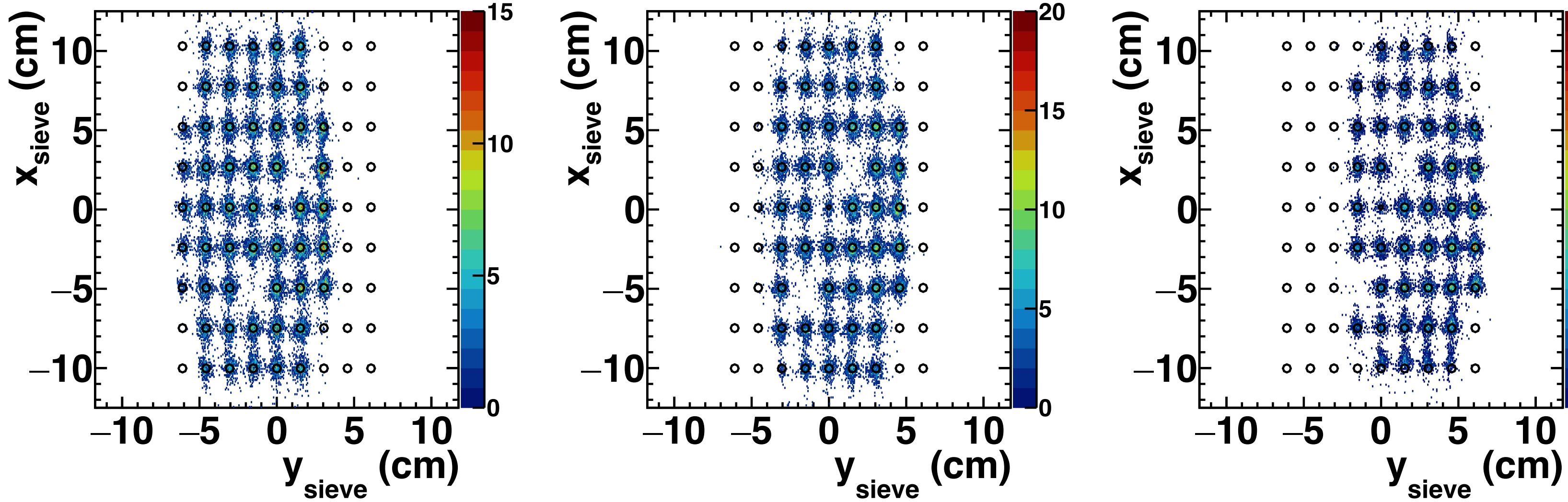

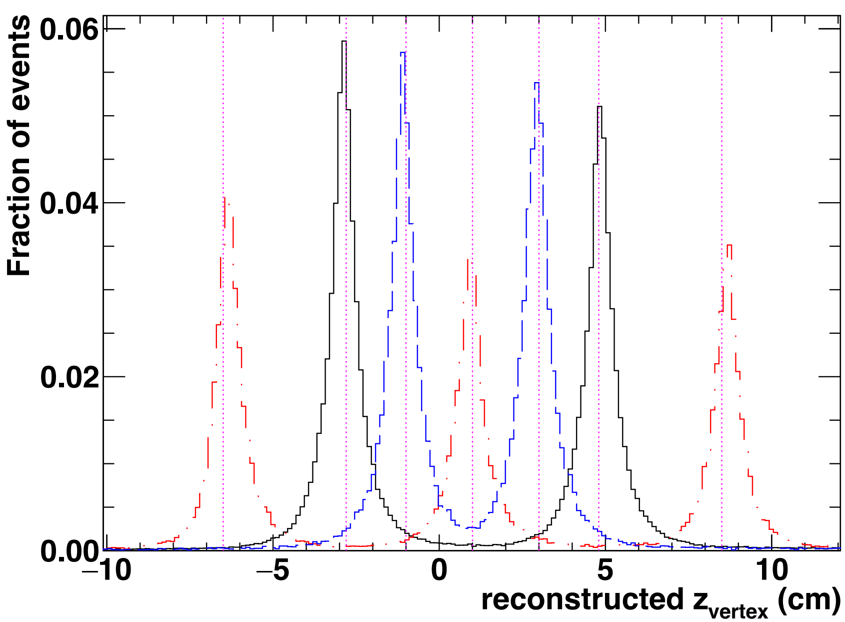

- Available optics targets in GEp-III:
  - 3-foil Al, $z = \pm 7.5\ cm, 0\ cm$
  - 2-foil C, $z = \pm 2\ cm$
  - 2-foil Al, $z = \pm 3.8$ cm
  - 20-cm Al "dummy", $z = 3.84 \pm 10$ cm
  - 15-cm Al "dummy", $z = \pm 7.5$ cm
- Most optics data were taken at 22-degree central angle, 2.4 GeV momentum, inelastically scattered electrons, beam energy 4.11 GeV
- Subset of runs taken at angles of 26 and 30 degrees, p = 2.15 and 1.9 GeV, resp.
- New, more "user-friendly" ROOT-based optics calibration code developed for this analysis.

HMS Optics Calibration results—Angle/Vertex resolution

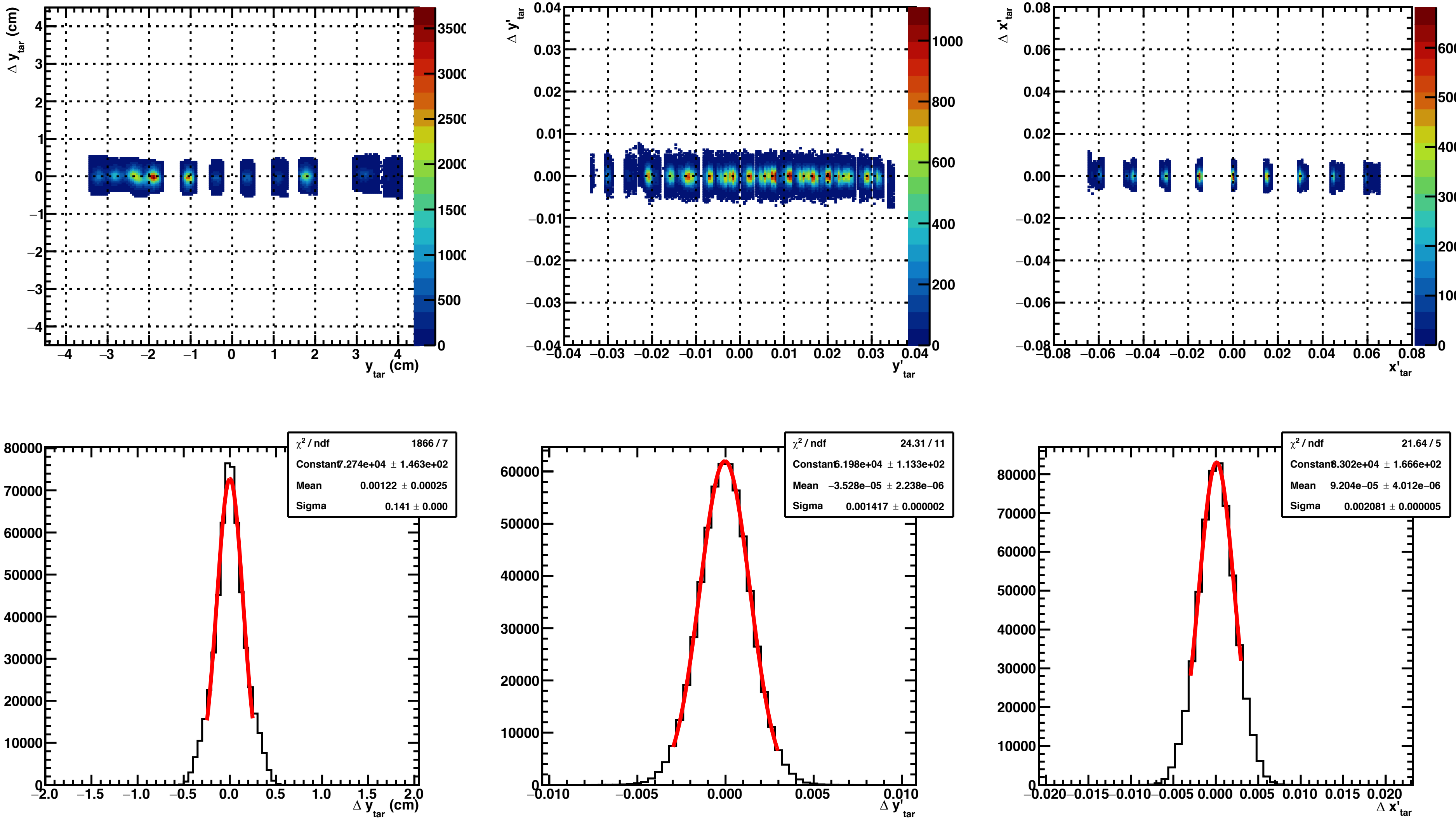

These resolutions are obtained for 2.4 GeV electrons, no “S0” in front of HMS drift chamber

HMS Optics Calibration: Momentum Reconstruction

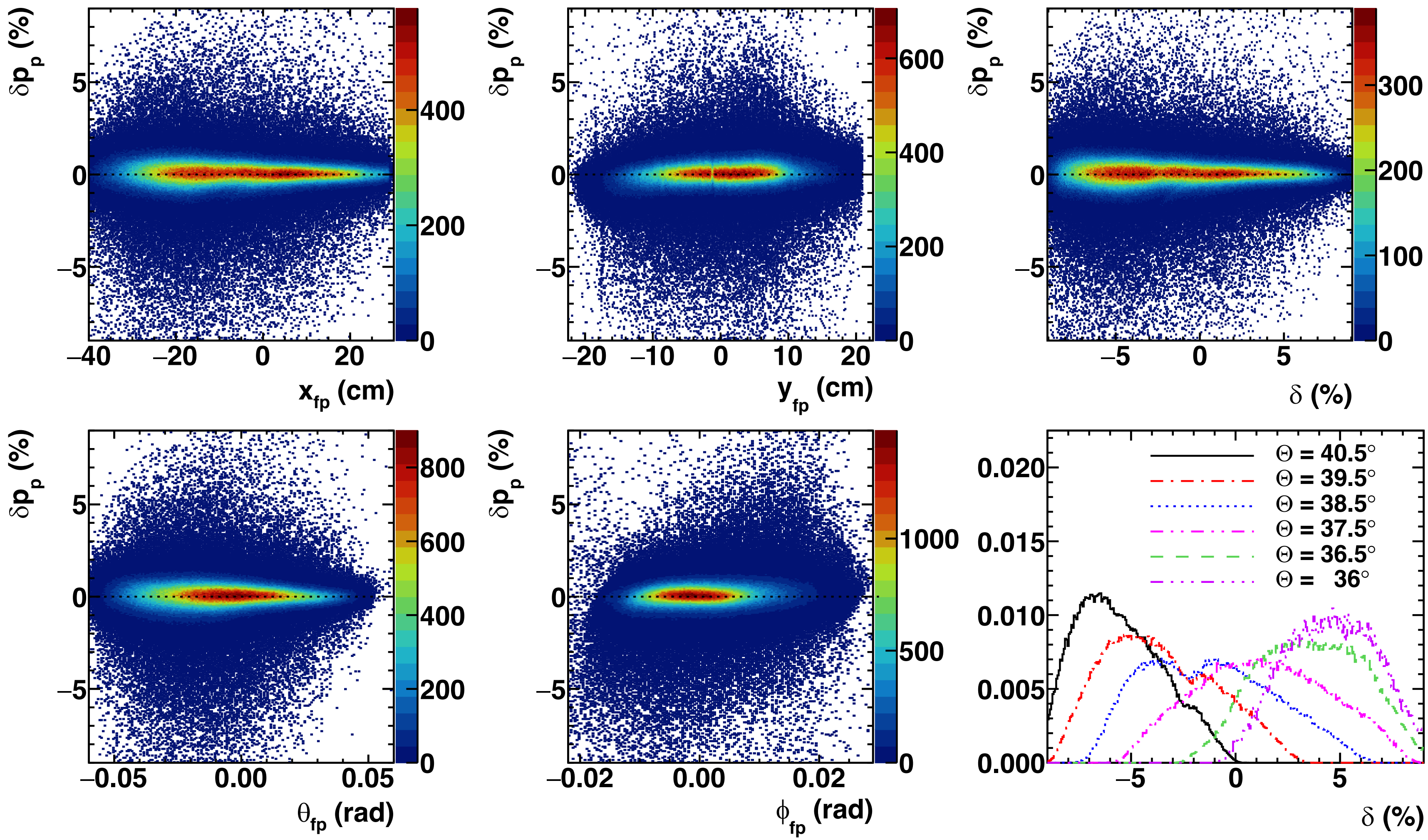

No new calibration of the δ matrix elements was attempted, based on good δ scan results with HMS detecting elastically scattered protons at E = 4.11 GeV, p = 2.02 GeV

Limitations of GEp-III Optics Data

- Our goal was to obtain a calibration of the HMS angle and/or vertex reconstruction that was well-behaved over the widest possible phase space, as the spin transport calculation is particularly sensitive to the scattering angle reconstruction.
- It proved difficult to obtain optics calibration data populating the full HMS acceptance due to the extended target length and the large HMS scattering angle (31, 35.4, and 36.1 deg for the high-ϵ kinematics of GEp-2γ: $\epsilon = 0.638, 779, 796$, respectively).
- For the high-Q^2 kinematics and for $\epsilon = 0.153$, the new calibration easily covers the full phase space populated by elastically scattered protons.
- For the aforementioned high-ϵ kinematics, some modest extrapolation outside the phase space directly constrained by optics data was required to use the full statistics.

FPP drift chamber design

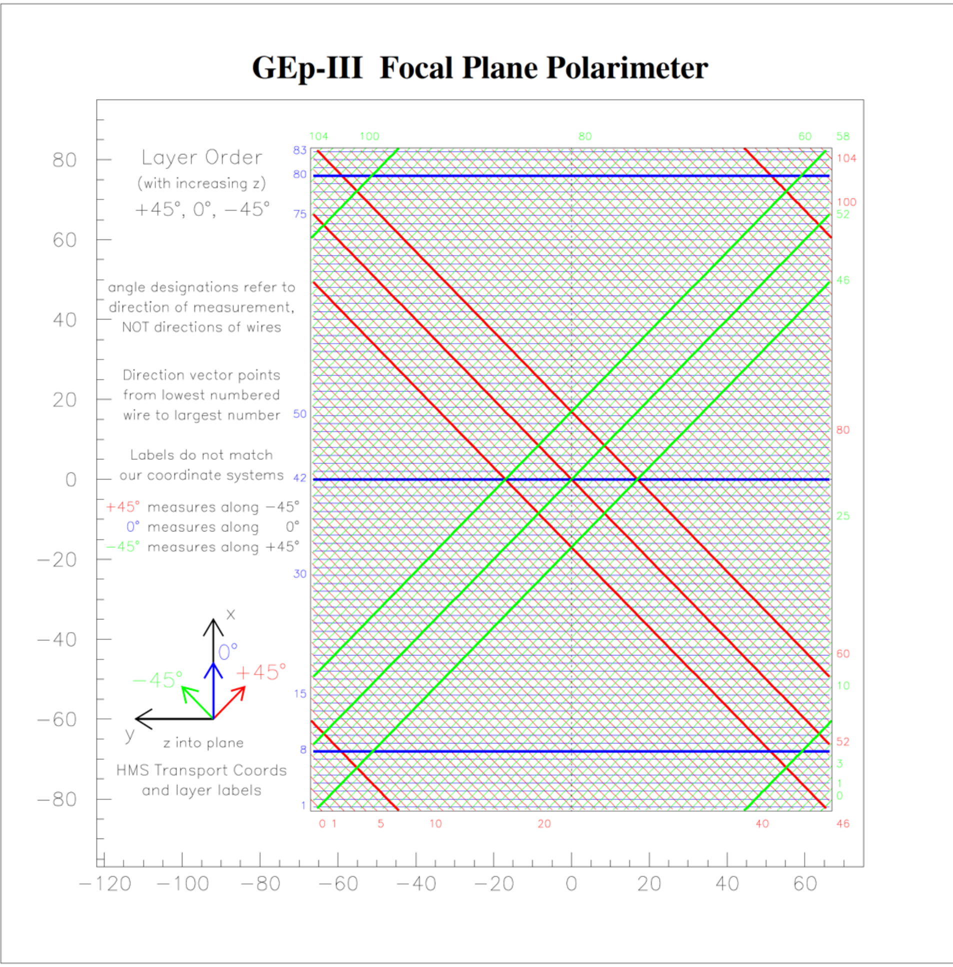

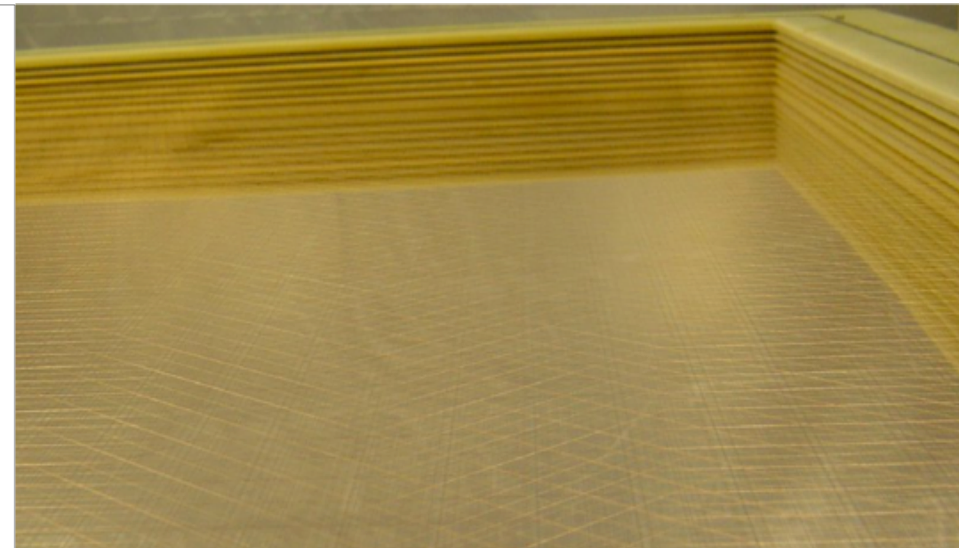

TABLE III. Characteristics of the wires used in the FPP drift chambers. The sense wires are gold-plated tungsten, while the cathode and field wires are made of a beryllium-bronze alloy.

Type	Diameter (μm)	Tension (g)
Sense	30	70
Field	100	150
Cathode	80	120

- Each chamber consists of three planes of sense wires, oriented at $\pm 45°, 90°$ relative to HMS dispersive direction, with 2-cm "pitch"
- Protons tracked after each analyzer by a pair of FPP chambers, ***six planes in total***

- FPP chambers and CH_2 analyzers are on separate support frames, to insure that FPP chambers cannot move upon insertion/retraction of the CH_2 analyzers
- Space in the HMS hut, cost considerations/etc limited the number of wire planes used for FPP tracking system.

FPP performance: coordinate and angular resolution

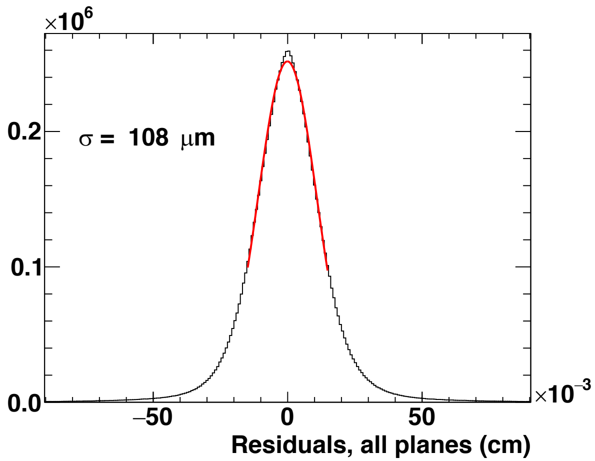

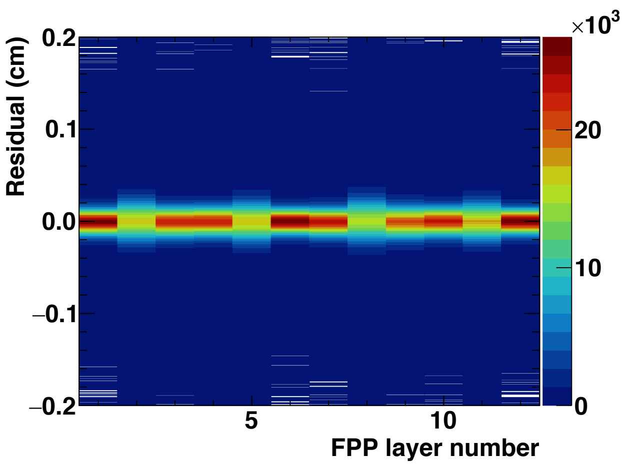

- Width of tracking residuals for straight-through tracks with all six planes firing average about 100 μm for 2.4 GeV electrons, slightly worse for 2.1-5.4 GeV protons.

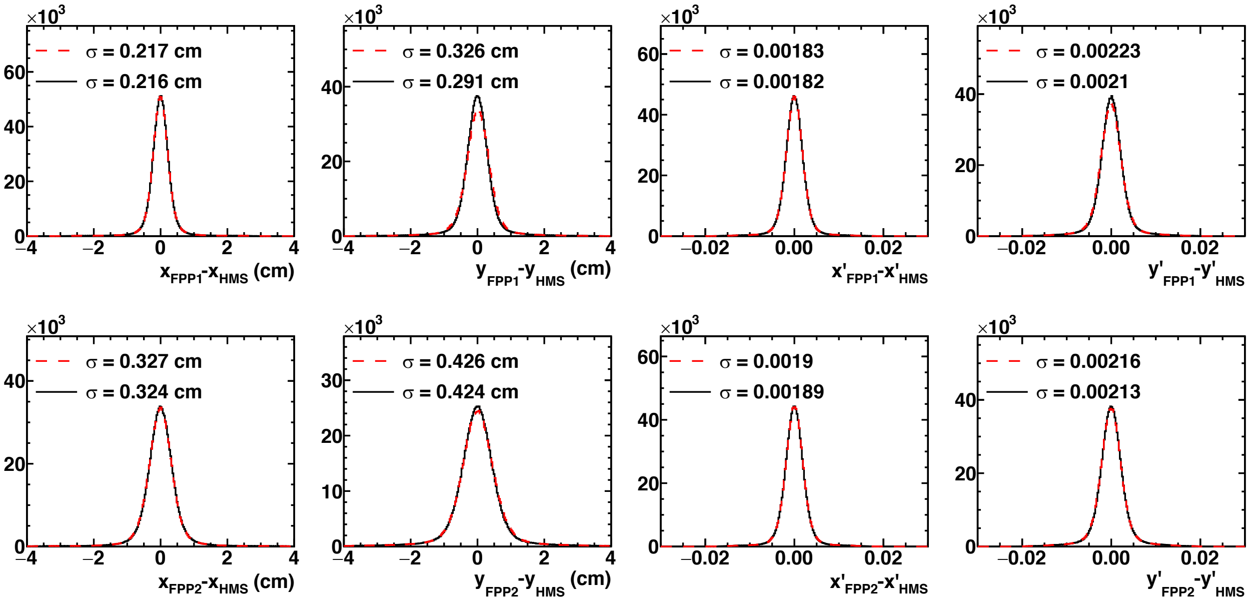

FPP-HMS track parameter differences, **before** (**after**) alignment corrections

- Observed tracking residuals correspond to an intrinsic coordinate resolution of $\approx 270\ \mu$m, which is consistent with observed HMS drift chamber resolution (same gas mixture, similar electric field/drift velocity/readout characteristics)
- As measured by track slope differences between FPP/HMS for straight-through tracks, FPP angular resolution is $\sigma_{x'}(\sigma_{y'}) = 1.8\ (2.1)$ mrad. The resolution asymmetry between the “x” and “y” directions results from the orientation/layout of the wire planes.
- The smallest polar scattering angle accepted in the analysis is ~0.5 degrees = 9 mrad (for $Q^2 = 8.5\ GeV^2$, $p_p = 5.4$ GeV/c)

FPP event selection criteria

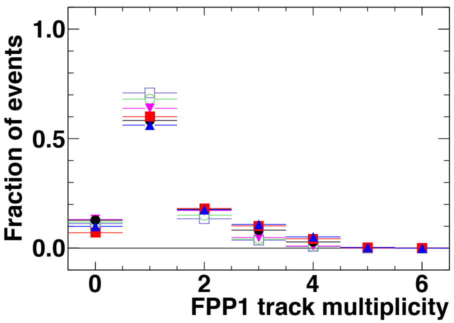

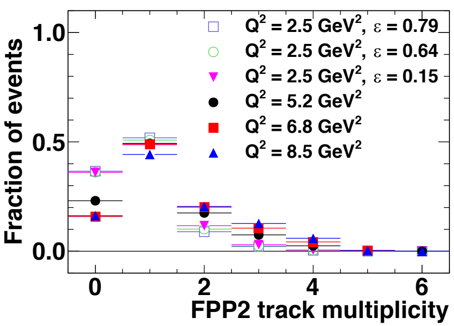

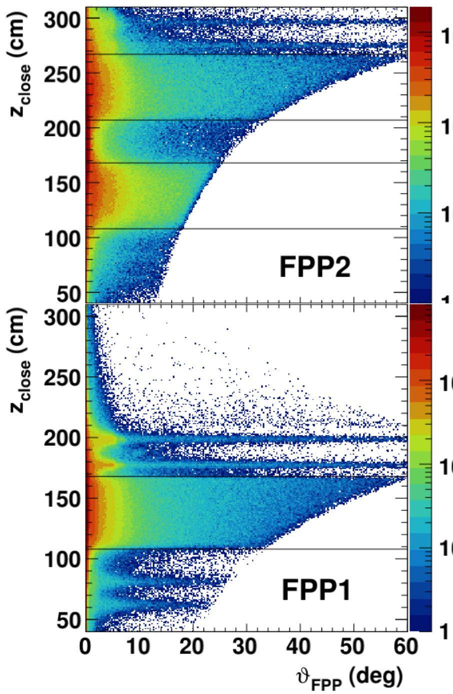

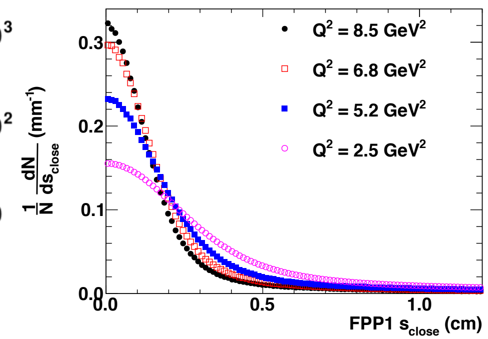

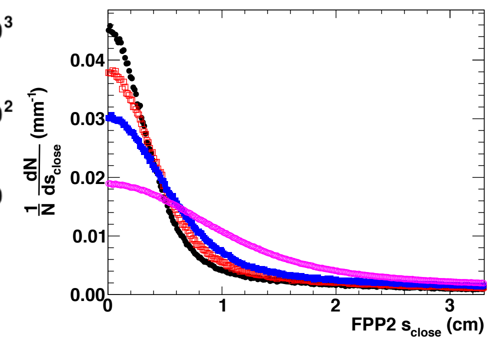

Table 1: FPP event selection criteria as a function of Q^2. Only single-track events passing the "cone test" were included in the analysis. No explicit ϑ cuts were applied. Instead, the ϑ ranges shown are the effective ranges resulting from the p_T cuts. The same criteria were applied to all three ϵ values at $Q^2 = 2.5$ GeV^2. s_{close} and z_{close} are defined, respectively, as the distance of closest approach between the incident and scattered tracks, and the z-coordinate of the point of closest approach between incident and scattered tracks, with $z = 0$ at the HMS focal plane.

Q^2 (GeV^2)	2.5	5.2	6.8	8.5
p_T^{min} (GeV/c)	0.06	0.05	0.05	0.05
p_T^{max} (GeV/c)	1.2	1.5	1.5	1.5
FPP1 ϑ^{eff}_{min} (°)	1.71	0.81	0.65	0.53
FPP1 ϑ^{eff}_{max} (°)	36.7	25.1	19.9	16.3
FPP2 ϑ^{eff}_{min} (°)	1.82	0.84	0.67	0.55
FPP2 ϑ^{eff}_{max} (°)	39.5	26.0	20.4	16.6
FPP1 s^{max}_{close} (cm)	2.2	1.7	1.4	1.2
FPP2 s^{max}_{close} (cm)	6.5	5.1	4.1	3.3
FPP1 z^{min}_{close} (cm)	108	108	108	108
FPP1 z^{max}_{close} (cm)	168	168	168	168
FPP2 z^{min}_{close} (cm)	207	207	207	207
FPP2 z^{max}_{close} (cm)	267	267	267	267

$$p_T \equiv p_p \sin\vartheta$$

- Useful events in the FPP are selected according to the following criteria:
  - Single charged track—multi-track events have low analyzing power, negligible contribution to figure-of-merit
  - Tracks must pass "cone test", requiring the projection of the cone of opening angle ϑ from the point of closest approach between incident and scattered tracks to the rearmost wire plane to be entirely contained within the FPP drift chamber active area (the z-dependent large-ϑ cutoff in the (ϑ, z_{close}) plot is due to the cone test application.
  - Distance of closest approach s_{close} between incident and scattered tracks is required to be less than a reasonable upper limit, chosen to optimize figure-of-merit
  - z_{close}, the "z" coordinate of the point of closest approach between incident and scattered tracks, must lie within the physical extent of the analyzer, with a small additional tolerance to account for detector resolution

FPP polar angle distributions

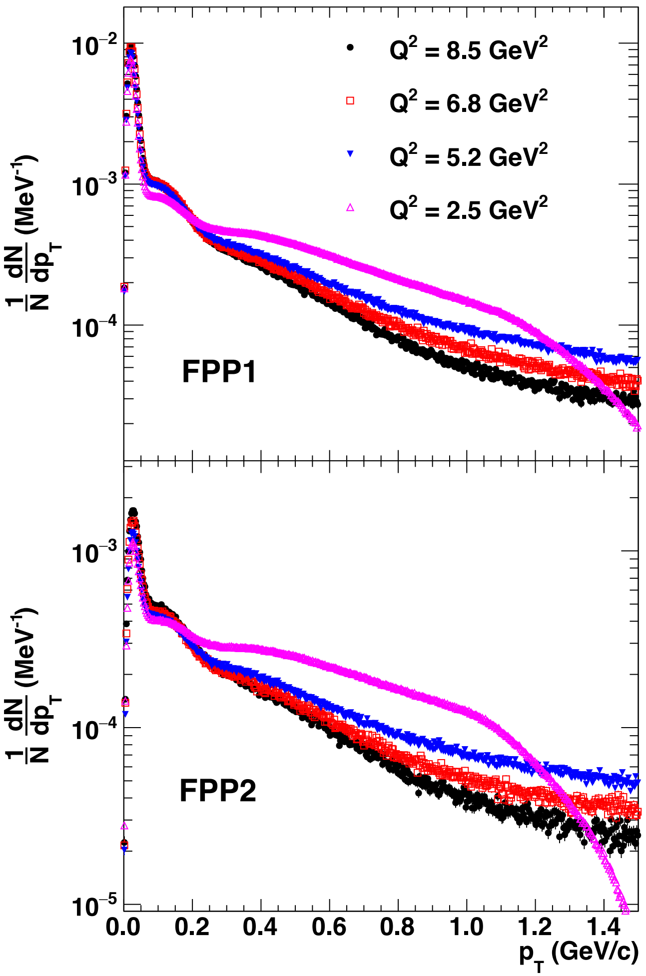

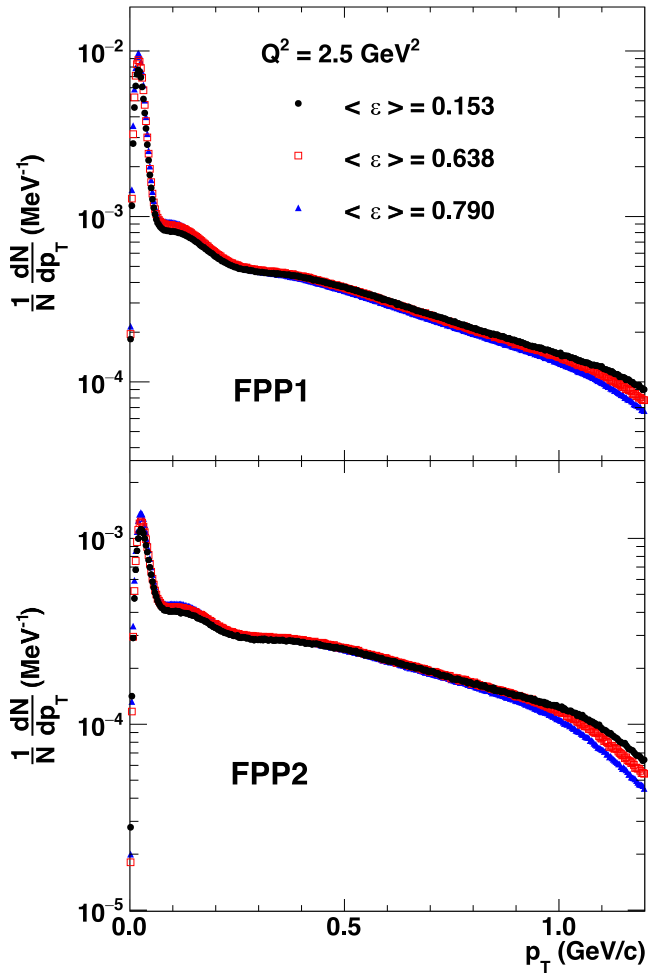

Table 1: FPP event selection criteria as a function of Q^2. Only single-track events passing the "cone test" were included in the analysis. No explicit ϑ cuts were applied. Instead, the ϑ ranges shown are the effective ranges resulting from the p_T cuts. The same criteria were applied to all three ϵ values at $Q^2 = 2.5$ GeV^2. s_{close} and z_{close} are defined, respectively, as the distance of closest approach between the incident and scattered tracks, and the z-coordinate of the point of closest approach between incident and scattered tracks, with $z = 0$ at the HMS focal plane.

Q^2 (GeV^2)	2.5	5.2	6.8	8.5
p_T^{min} (GeV/c)	0.06	0.05	0.05	0.05
p_T^{max} (GeV/c)	1.2	1.5	1.5	1.5
FPP1 ϑ_{min}^{eff} (°)	1.71	0.81	0.65	0.53
FPP1 ϑ_{max}^{eff} (°)	36.7	25.1	19.9	16.3
FPP2 ϑ_{min}^{eff} (°)	1.82	0.84	0.67	0.55
FPP2 ϑ_{max}^{eff} (°)	39.5	26.0	20.4	16.6
FPP1 s_{close}^{max} (cm)	2.2	1.7	1.4	1.2
FPP2 s_{close}^{max} (cm)	6.5	5.1	4.1	3.3
FPP1 z_{close}^{min} (cm)	108	108	108	108
FPP1 z_{close}^{max} (cm)	168	168	168	168
FPP2 z_{close}^{min} (cm)	207	207	207	207
FPP2 z_{close}^{max} (cm)	267	267	267	267

$$p_T \equiv p_p \sin\vartheta$$

- Coulomb scattering dominates for $p_T \leq 0.06$ GeV
- Analyzing power negligible for $p_T \geq 1$ GeV

- Polar scattering angle distribution *approximately* scales with proton momentum, for a given CH_2 thickness.
- At $Q^2 = 2.5\ GeV^2$, the p_T distributions are the same for all three kinematics, at the few-percent level, as expected.

FPP azimuthal asymmetries, I

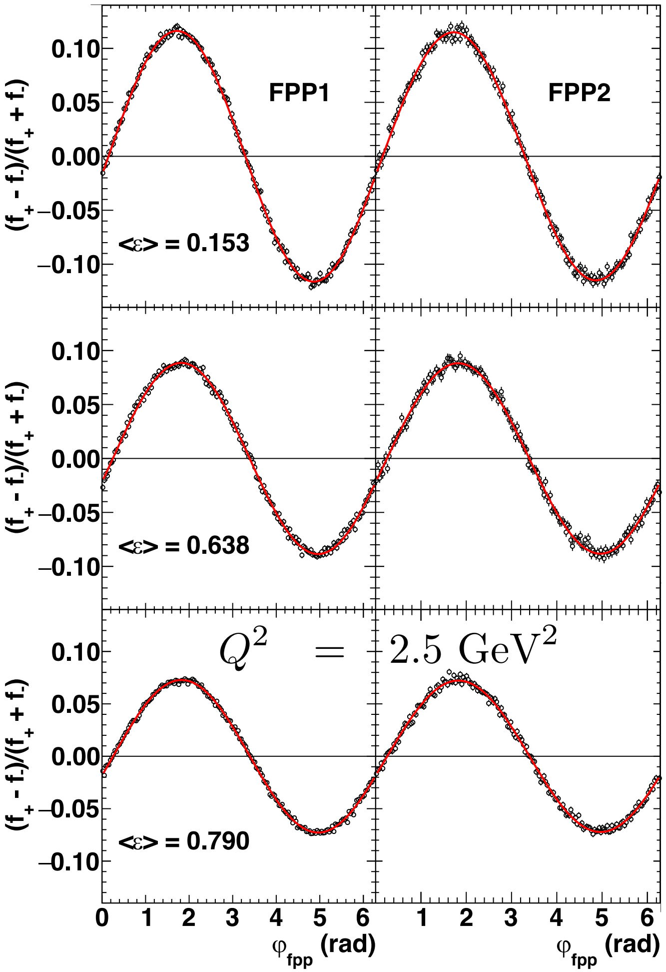

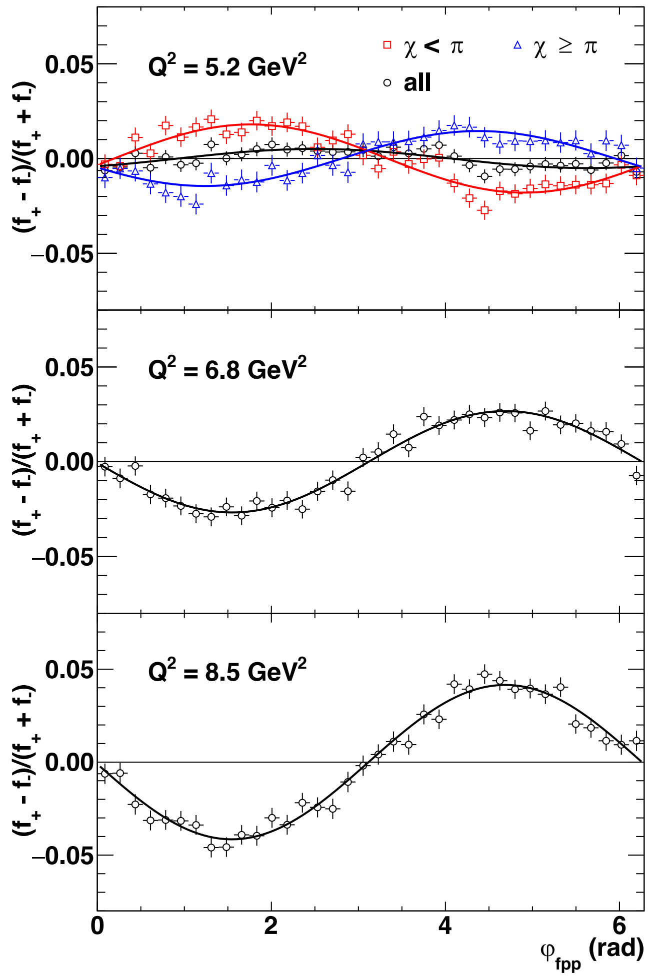

- The 30-Hz beam helicity reversal cancels the effects of FPP instrumental asymmetries due to; e.g., φ-dependence of acceptance and/or efficiency and/or angular resolution
- The resulting sinusoidal asymmetry is proportional to the effective average analyzing power of the selection of events and the incident proton's transverse polarization components.
- Only the transferred polarization components survive in the difference distribution between opposite beam helicity states
- The proton's polarization at the focal plane is related to the reaction-plane transferred polarization components P_t, P_ℓ by a rotation describing the spin transport through the HMS magnetic field.

$$\frac{f_+ - f_-}{f_+ + f_-} = \frac{\bar{A}_y \left(P_{y,tr}^{FPP} \cos\varphi - P_{x,tr}^{FPP} \sin\varphi\right)}{1 + \bar{A}_y \left(P_{y,ind}^{FPP} \cos\varphi - P_{x,ind}^{FPP} \sin\varphi\right)} \approx \bar{A}_y \left(P_{y,tr}^{FPP} \cos\varphi - P_{x,tr}^{FPP} \sin\varphi\right) \qquad (20)$$

FPP azimuthal asymmetries, II

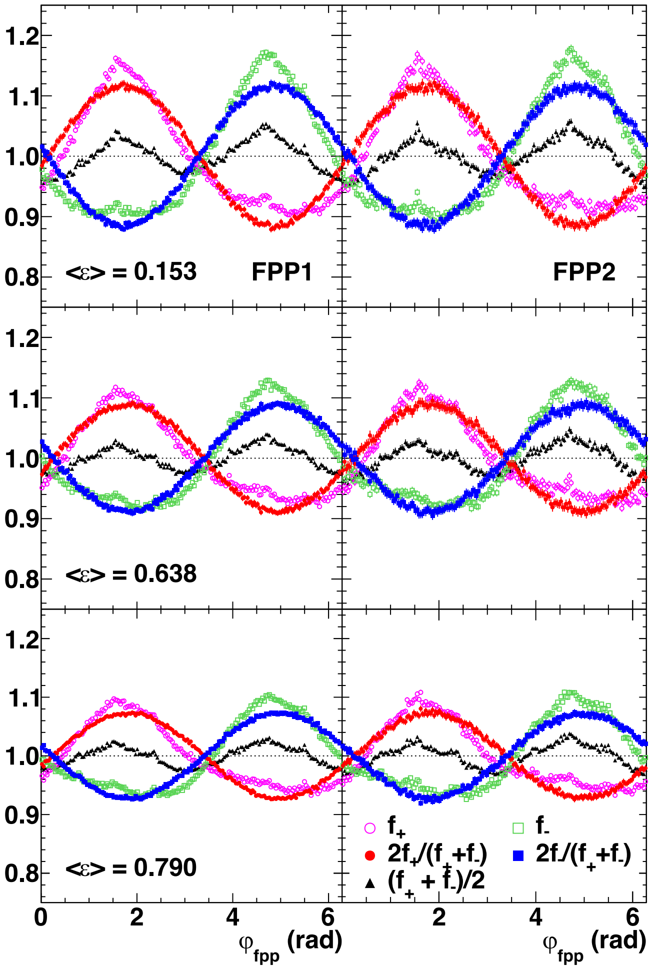

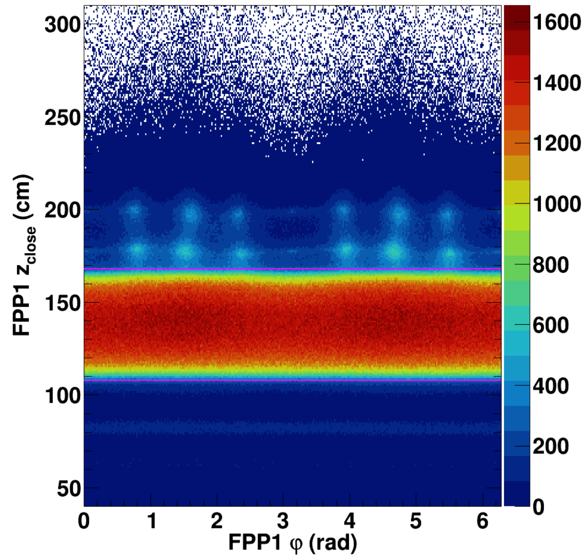

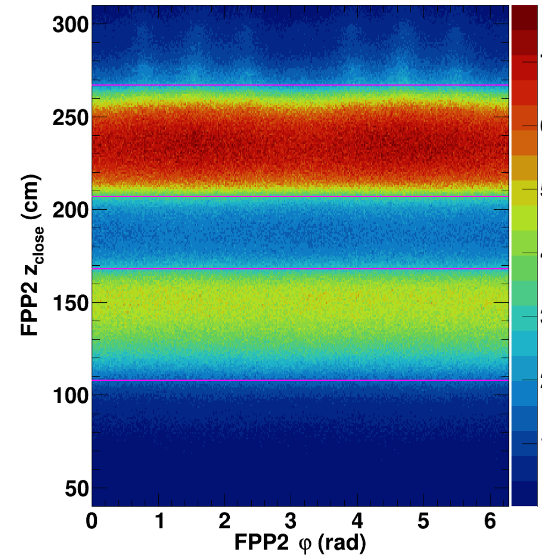

- Spurious, artificial peaks in the helicity-sum φ spectrum, at angles corresponding to FPP wire orientations, and z_{close} corresponding to the drift chamber locations, result from incorrect solutions of the left-right ambiguity (see next slide)
- These events are mostly (but not entirely) rejected by the z_{close} cuts.

$$\begin{aligned} f^+ + f^- &\equiv \frac{\pi}{\Delta\varphi}\left[\frac{N^+(\varphi)}{N_0^+} + \frac{N^-(\varphi)}{N_0^-}\right] \\ &= [1+\mu_0(\varphi)] \times \\ &\quad [1+\bar{A}_y(P^{FPP}_{y,ind}\cos\varphi - P^{FPP}_{x,ind}\sin\varphi)] \\ &\approx 1+\mu_0(\varphi) \qquad (19) \end{aligned}$$

$$\mu_0(\varphi) \equiv \sum_{n=1}^{\infty}\left[c_n\cos(n\varphi) + s_n\sin(n\varphi)\right]$$

$$\begin{aligned} \frac{2f_\pm}{f_+ + f_-} &= 1 \pm \frac{\bar{A}_y\left(P^{FPP}_{y,tr}\cos\varphi - P^{FPP}_{x,tr}\sin\varphi\right)}{1+\bar{A}_y\left(P^{FPP}_{y,ind}\cos\varphi - P^{FPP}_{x,ind}\sin\varphi\right)} \\ &\approx 1 \pm \bar{A}_y\left(P^{FPP}_{y,tr}\cos\varphi - P^{FPP}_{x,tr}\sin\varphi\right) \qquad (21) \end{aligned}$$

Irreducible FPP left-right ambiguity

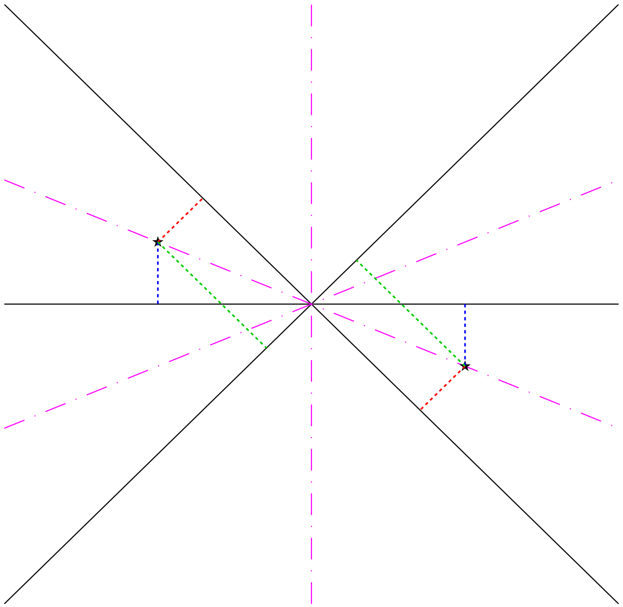

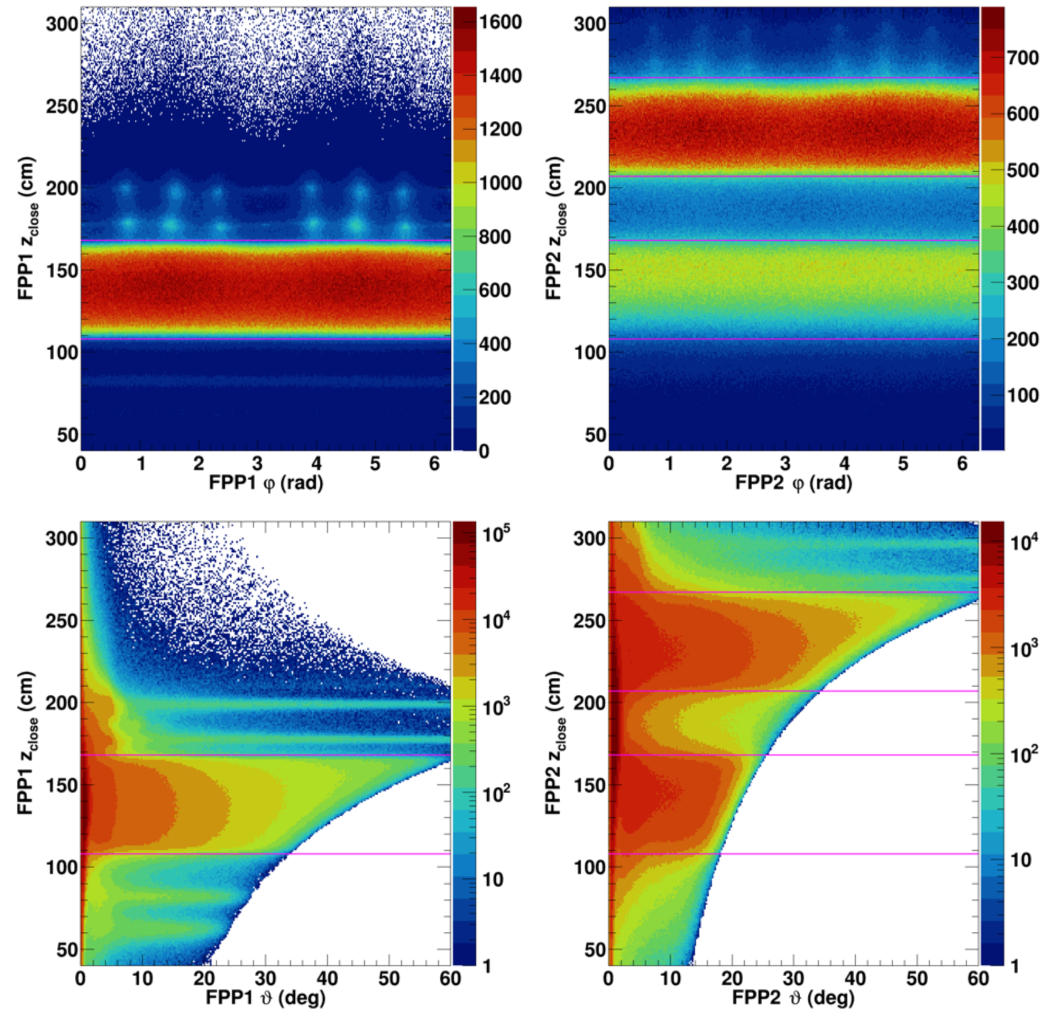

- The symmetry of wire orientations and common intersection point of U, V, X wires at chamber center leads to the existence of two solutions with (nearly) identical χ^2, with hits placed on the opposite side of all three wires firing in a given chamber, for tracks at or near normal incidence.
- Ambiguity cannot be eliminated without introducing scattering-parameter-dependent biases in the pattern recognition and track reconstruction, which is dangerous.
- Ambiguity can be eliminated (for future experiments) by adding more wire planes; e.g., operating in a single-FPP configuration with 12 tracking planes by retracting the second analyzer block, or retaining the double-FPP layout, but slightly reducing the thickness of each analyzer block and adding a third identical chamber to each FPP.

Analyzing Power Calibration

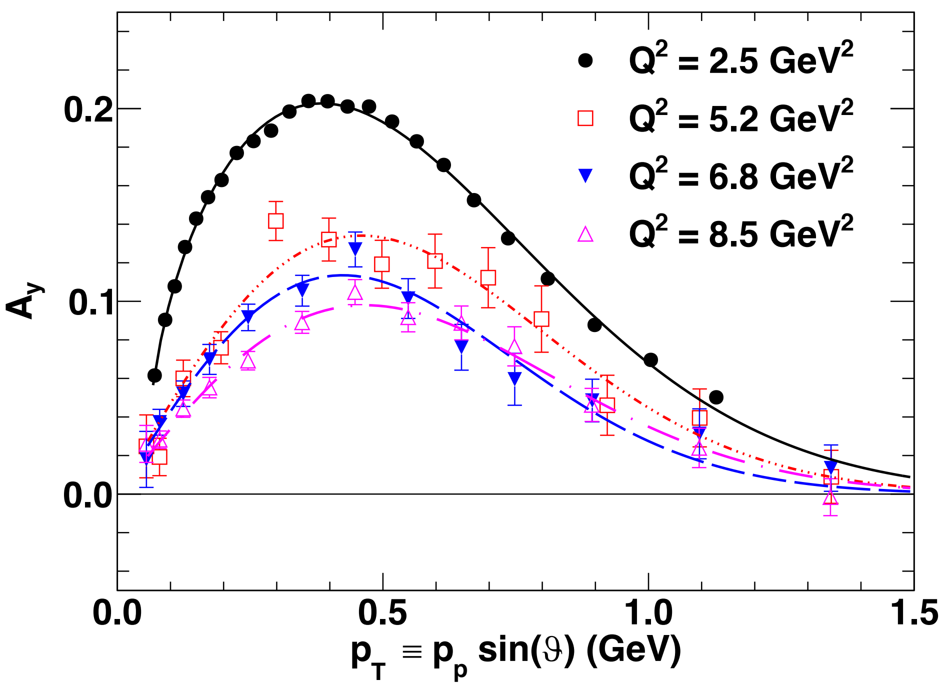

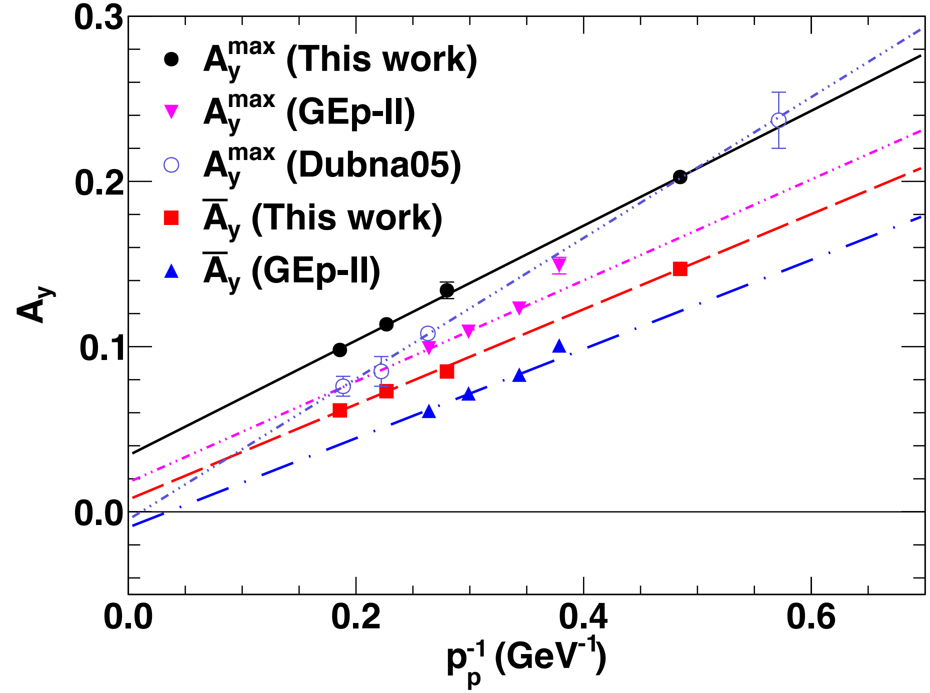

$$\hat{P}_t^{(A_y=1)} = \bar{A}_y P_t$$

$$\hat{P}_\ell^{(Ay=1)} = \bar{A}_y P_\ell$$

$$\bar{A}_y = \frac{\hat{P}_t^{(A_y=1)}}{P_t^{Born}} = \frac{\hat{P}_\ell^{(A_y=1)}}{P_\ell^{Born}}$$

$$A_y(p_p, p_T) = A_y^0(p_T)\frac{\bar{p_p}}{p_p},$$

- The analyzing power distribution in terms of $p_T = p_p \sin\vartheta$ is roughly Q^2-independent, up to an overall normalization constant, with a maximum at $p_T \approx 0.4$ GeV.
- Both the maximum and the average (for equivalent p_T ranges) analyzing power scale as p_p^{-1}.
- The analyzing power momentum dependence is corrected for event-by-event assuming an overall p_p^{-1} scaling, independent of ϑ.
- Hall C FPP effective A_y significantly exceeds that of other experiments using CH_2. This is attributable to the capability to isolate true single-track events, absent from Hall A and Dubna measurements

HMS Spin Transport, I

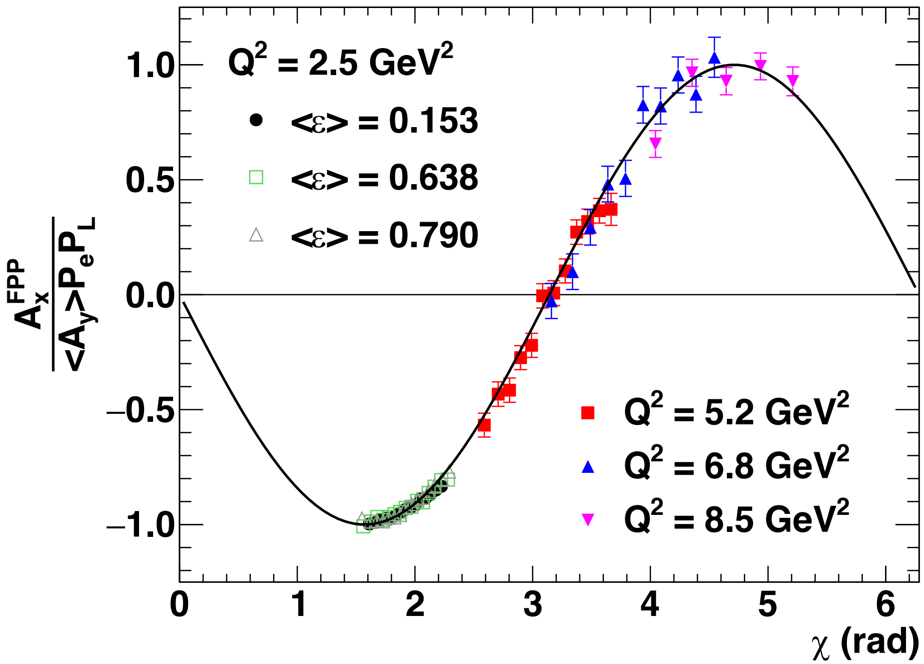

$$A_x^{FPP} \approx -\sin\chi \langle A_y \rangle P_e P_\ell$$

- The ideal dipole approximation qualitatively accounts for the acceptance-averaged behavior of the sin φ asymmetry A_x^{FPP}.
- The wide χ acceptance of the HMS provides adequate sensitivity to P_ℓ even at $Q^2 = 5.2$ GeV^2, for which the acceptance-averaged asymmetry is close to zero.

- The precession of the polarization of relativistically moving charged particles in a magnetic field is described in the lab frame by the Thomas-BMT equation: Phys. Rev. Lett. 2, 435 (1959).
- For protons, the equation can be written as:

$$\frac{d\mathbf{S}}{dt} = \frac{e}{\gamma m}\mathbf{S} \times \left(\frac{g}{2}\mathbf{B}_\parallel + \left[1 + \gamma\left(\frac{g}{2} - 1\right)\right]\mathbf{B}_\perp\right)$$
$$\frac{d\mathbf{v}}{dt} = \frac{e}{\gamma m}\mathbf{v} \times \mathbf{B}$$

- Here $B_\parallel$ and $B_\perp$ are the magnetic field components parallel and perpendicular to the proton's velocity, respectively, and g is the gyromagnetic ratio
- In the ideal dipole approximation, the proton spin component perpendicular to the HMS dipole field (which roughly coincides with P_ℓ) precesses by an angle $\chi = \gamma\kappa_p\theta_{bend}$ relative to the proton trajectory (where θ_{bend} is the trajectory bend angle), while the component parallel to the dipole field does not precess; i.e.:

$$P_y^{FPP} \approx P_t$$
$$P_x^{FPP} \approx -\sin\chi P_\ell$$

- The spin transport matrix is computed event-by-event from a detailed 5[th]-order COSY INFINITY model of the HMS including fringe fields.

HMS Spin Transport, II

$$S_{yt} \approx \cos\chi_\phi$$
$$S_{y\ell} \approx \sin\chi_\phi$$
$$S_{xt} \approx \sin\chi_\phi \sin\chi$$
$$S_{x\ell} \approx -\cos\chi_\phi \sin\chi$$

$$\chi_\phi \equiv \gamma\kappa_p(\phi_{fp} - \phi_{tar}) \equiv \gamma\kappa_p\phi_{bend}$$
$$\chi \equiv \gamma\kappa_p\theta_{bend}$$

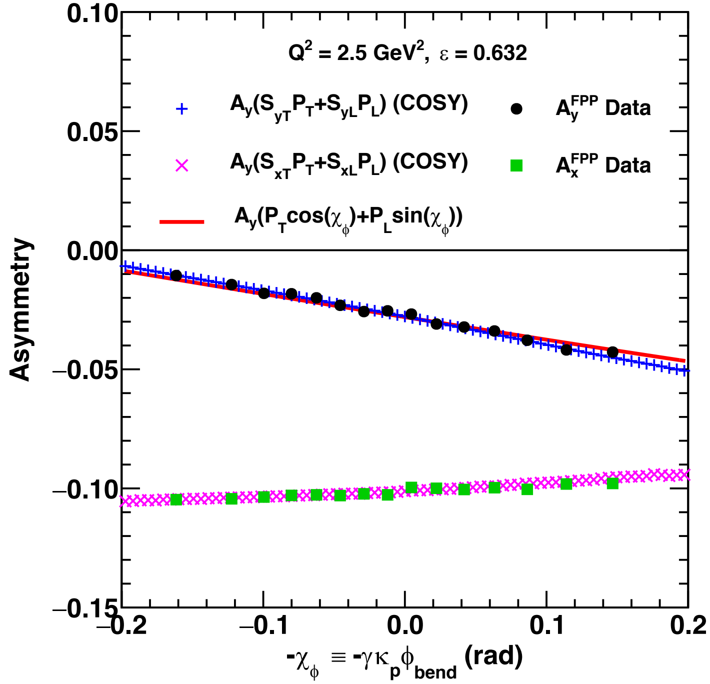

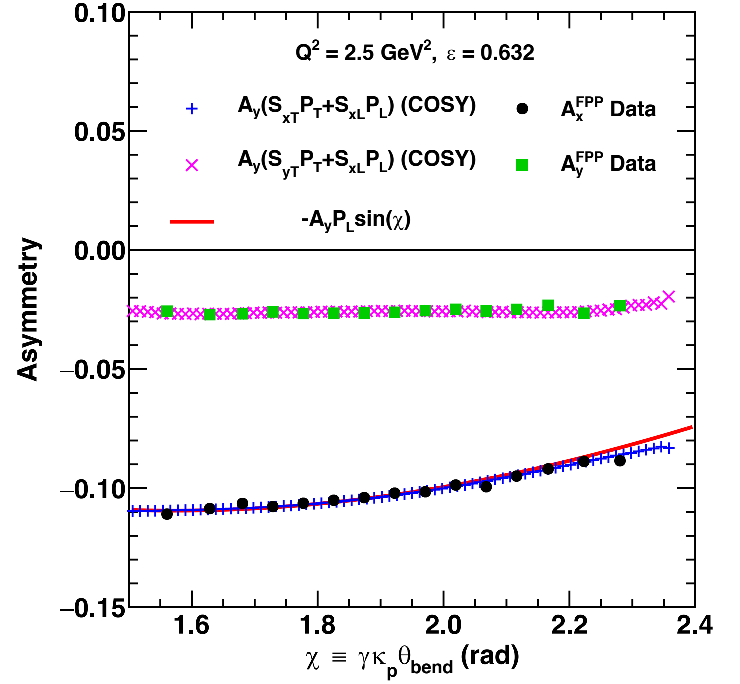

- The quadrupoles also cause the proton spin to precess in the non-dispersive (horizontal) plane, mixing P_t and P_ℓ.
- The total rotation relative to the trajectory can be approximated by the composition of a rotation by angle $\chi_\phi \equiv \gamma\kappa_p\phi_{bend}$ in the non-dispersive plane, followed by a rotation through angle χ in the dispersive (vertical) plane.
- For the HMS, the differences between this “geometric” approximation and the full COSY calculation are quite small, due to the ”simple” QQQD layout of the magnets.
- The observed χ, χ_ϕ dependencies of the measured FPP asymmetries are in good agreement with COSY and the geometric approximation

FPP azimuthal asymmetry definitions:

- A_y = analyzing power
- S_{ij}’s are spin transport matrix elements

$$\frac{f_+(\varphi) - f_-(\varphi)}{f_+(\varphi) + f_-(\varphi)} = A_y^{FPP}\cos\varphi - A_x^{FPP}\sin\varphi$$
$$A_y^{FPP} \equiv A_y P_y^{FPP} = A_y(S_{yt}P_t + S_{y\ell}P_\ell)$$
$$A_x^{FPP} \equiv A_y P_x^{FPP} = A_y(S_{xt}P_t + S_{x\ell}P_\ell)$$

Data quality checks ($\mu_p G_E^p / G_M^p$)—Analyzing power cancellation

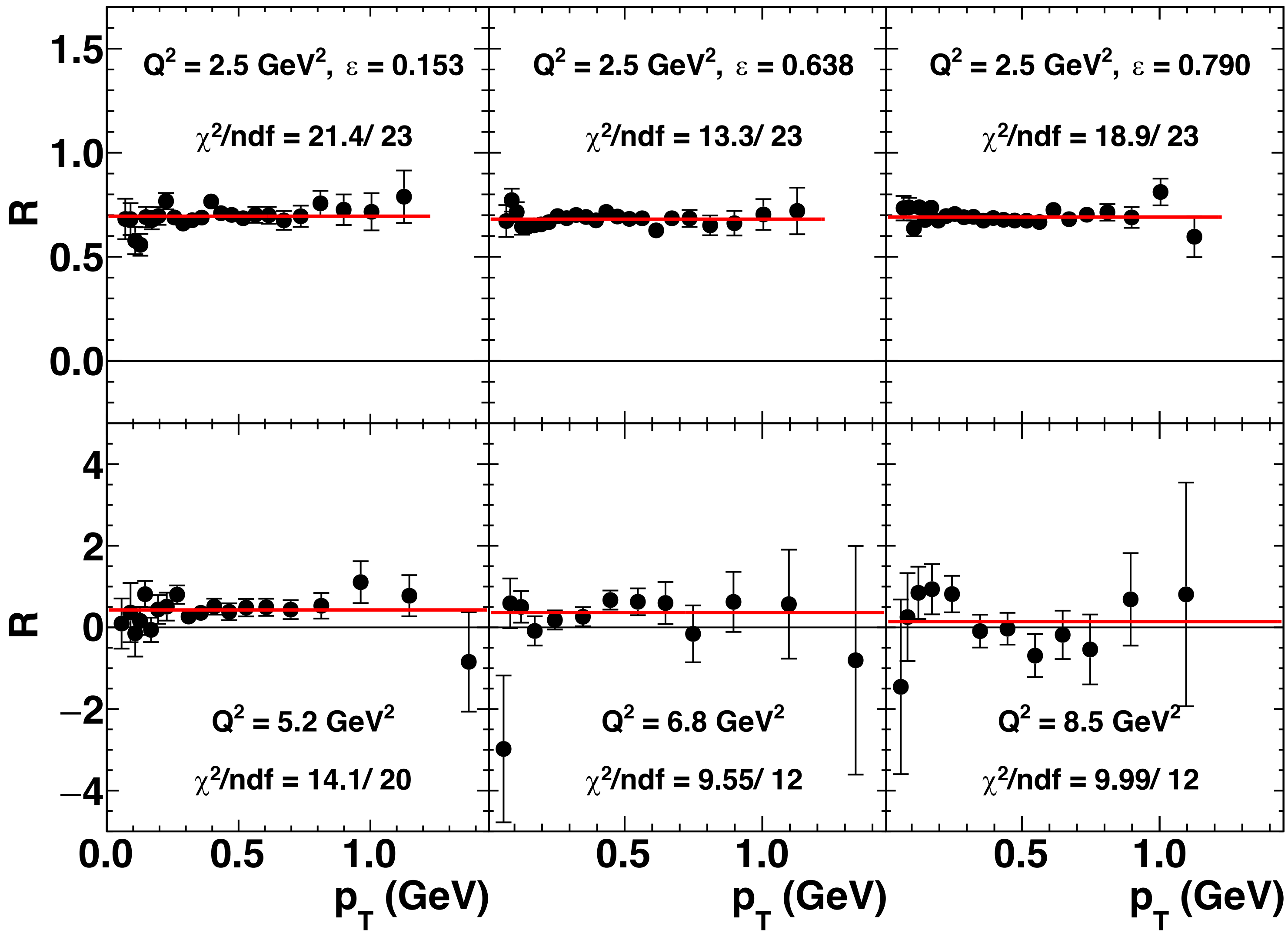

- The constancy of the extracted FF ratio as a function of $p_T = p_p \sin\vartheta$ confirms the cancellation of A_y in the ratio P_t/P_ℓ

Data quality checks ($\mu_p G_E^p / G_M^p$)—kinematic dependence

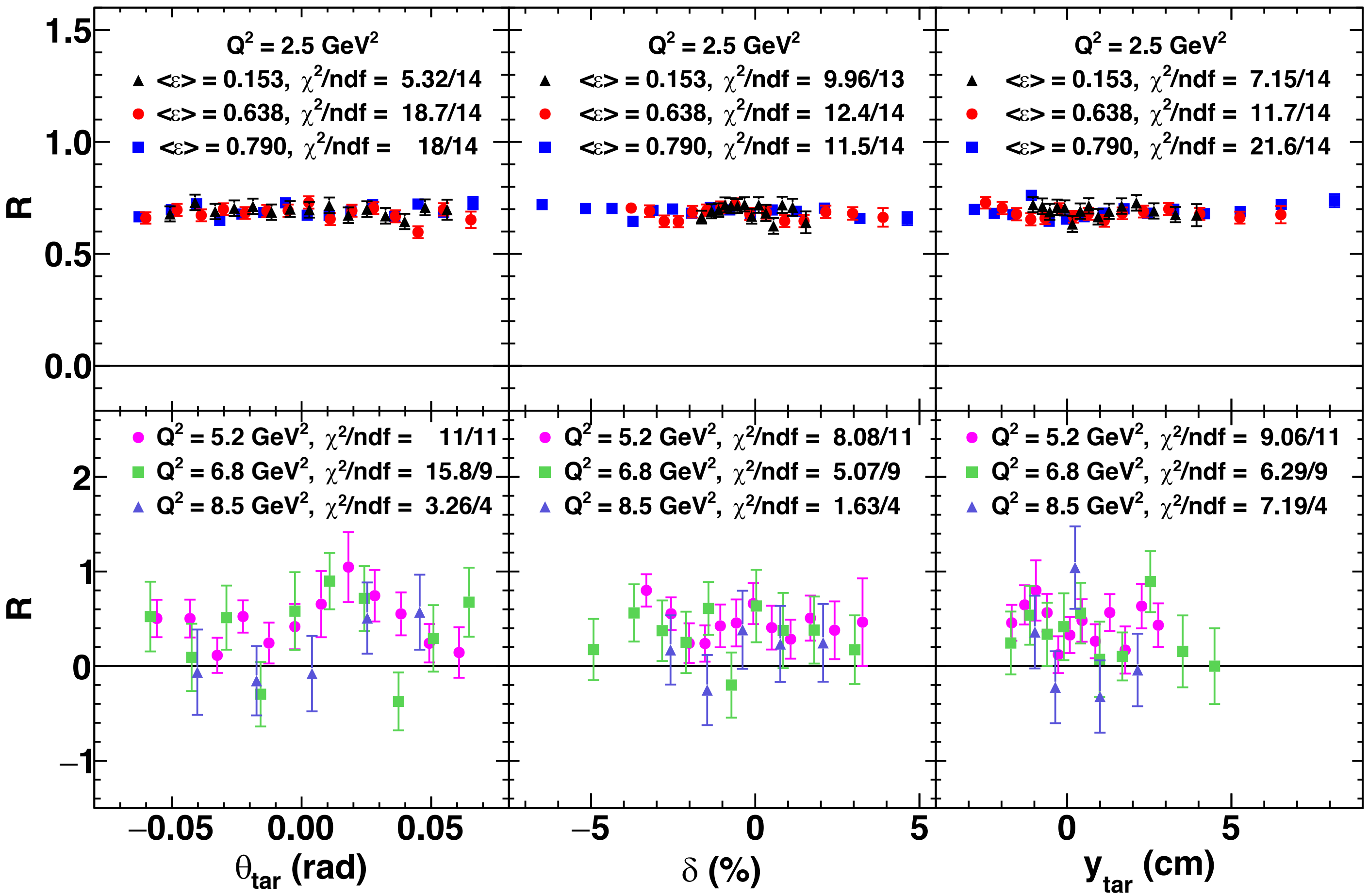

$$\chi^2 \equiv \sum_i \frac{\left(\frac{R_i}{R_0(Q_i^2)} - \bar{R}\right)^2}{\sigma_i^2},$$

$$\bar{R} \equiv \frac{\sum_j \frac{R_j}{\sigma_j^2 R_0(Q_j^2)}}{\sum_k \frac{1}{\sigma_k^2}},$$

$$\sigma_i^2 \equiv \left(\frac{\Delta R_i}{R_0(Q_i^2)}\right)^2,$$

- The absence of spurious dependence of the extracted FF ratio on the reconstructed proton kinematics validates the ML method for the extraction of R and the accuracy of the HMS optics and spin transport calculation.
- Here χ^2 is computed with respect to the ratio of R to its "expected" value based on a global proton FF fit, to account for the Q^2 dependence of R within the acceptance.

Data quality checks (P_ℓ / P_ℓ^{Born})—A_y momentum dependence

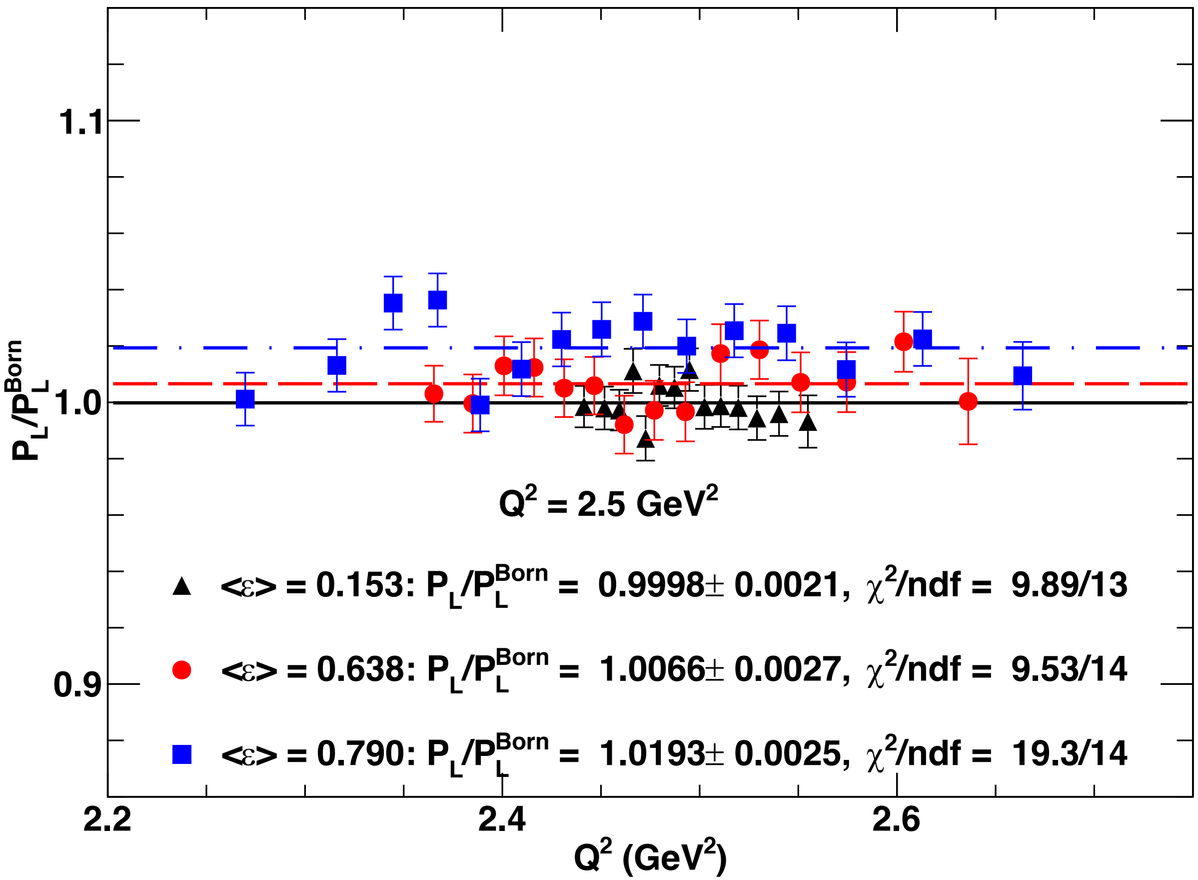

- The overall proton momentum dependence of the analyzing power is assumed to factorize from the angular dependence, according to:

$$A_y(p_p, p_T) = A_y^0(p_T)\frac{\bar{p_p}}{p_p},$$

- The application of identical cuts on the scattering parameters $s_{close}, z_{close}, p_T$ insures that the average analyzing power for the three ϵ values is the same, up to differences in the momentum distribution of incident protons.

- Measuring the *relative* ϵ dependence of P_ℓ / P_ℓ^{Born} at 2.5 GeV² relies on the assumption that the average analyzing power is the same for all three kinematics, up to an overall $\frac{1}{p_p}$ scaling which accounts for the differences in Q^2 acceptance/average Q^2 between the different kinematics.
- The lowest ϵ point is used to calibrate A_y under the assumption $P_\ell = P_\ell^{Born}$, since $P_\ell^{Born} \to 1$ as $\epsilon \to 0$, and is thus very insensitive to the FF ratio ($P_\ell^{Born} = 0.9753 \pm 0.0003$ at $< \epsilon > = 0.153$).

Data quality checks—Beam Polarization Database

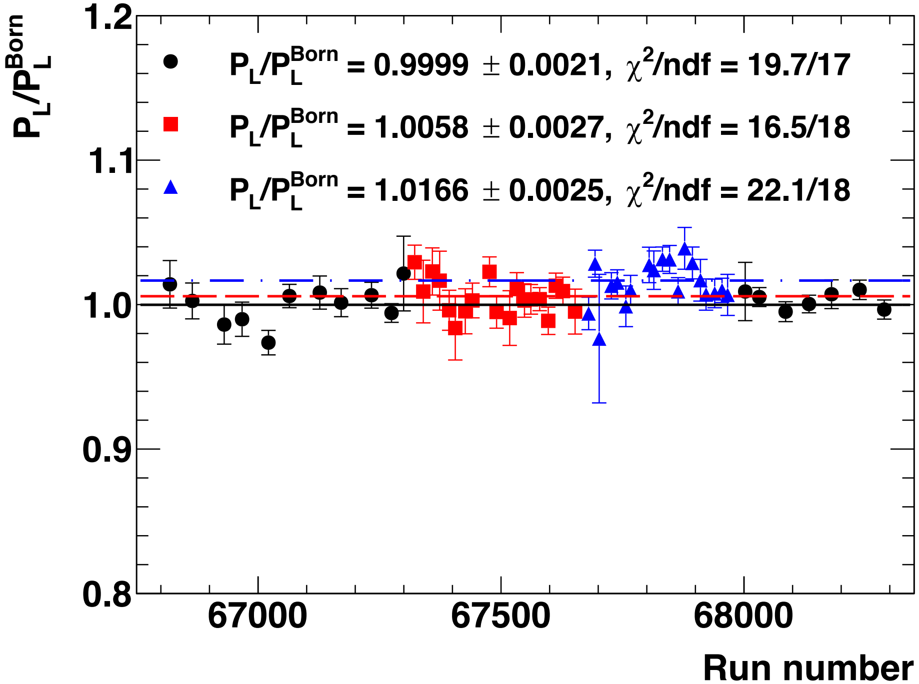

Extracted $\frac{P_\ell}{P_\ell^{Born}}$ vs. run number during GEp-2γ

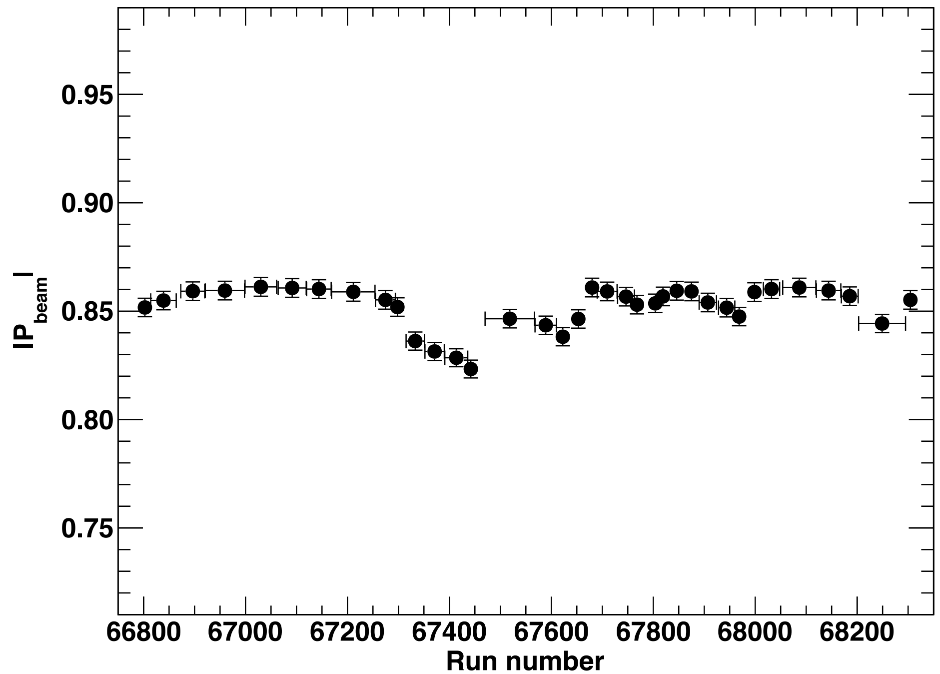

Moller measurements of beam polarization during GEp-2γ with associated run ranges

- Moller measurement of beam polarization was carried out roughly every 2 days during GEp-2γ. As an intrusive measurement, data taking had to be interrupted to measure polarization; no ”online” monitoring of beam polarization was possible, except via FPP asymmetry magnitude.
- Stability of extracted $\frac{P_\ell}{P_\ell^{Born}}$ confirms validity of beam polarization database and stability of beam polarization between Moller measurements.

HMS Spin Transport Systematics—non-dispersive plane

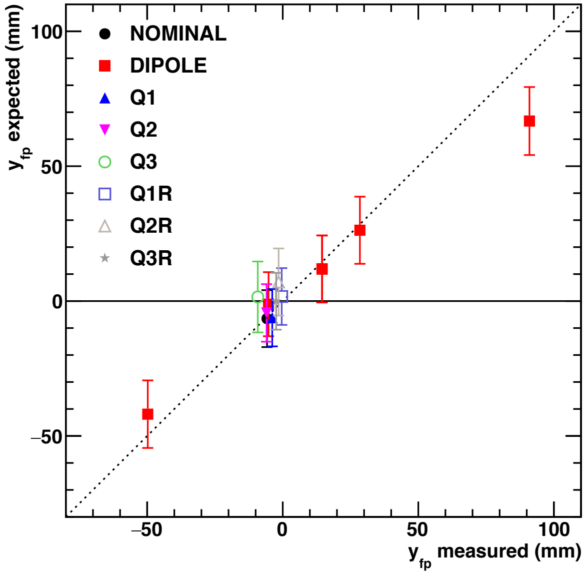

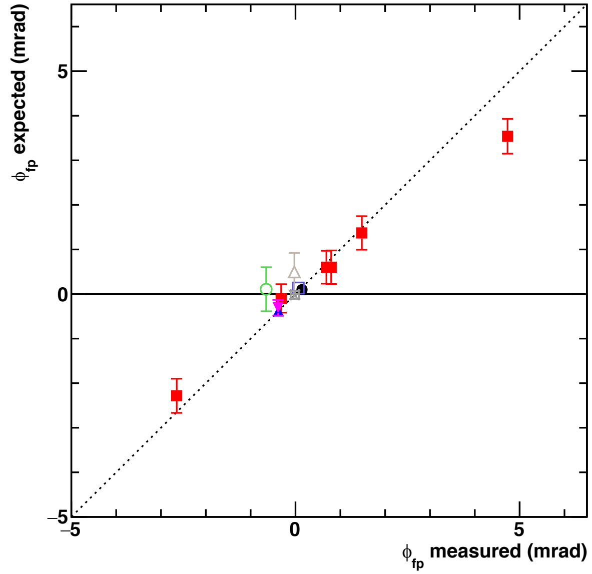

$$S_{yt} \approx \cos\chi_\phi$$
$$S_{y\ell} \approx \sin\chi_\phi$$
$$S_{xt} \approx \sin\chi_\phi \sin\chi$$
$$S_{x\ell} \approx -\cos\chi_\phi \sin\chi$$
$$\chi_\phi \equiv \gamma\kappa_p(\phi_{fp} - \phi_{tar}) \equiv \gamma\kappa_p\phi_{bend}$$
$$\chi \equiv \gamma\kappa_p\theta_{bend}$$

$$\phi^{(s)}_{bend} = \sum_i (\phi_{fp}|s_i)s_i$$
$$\phi^{(total)}_{bend} = \phi^{(s)}_{bend} + \phi_0^{fp} + (\phi_{fp}|y_{tar})y_0^{tar} + [(\phi_{fp}|\phi_{tar}) - 1]\frac{y_{sieve} - y_0^{tar}}{z_{sieve}},$$

$$R = -K\frac{P_t}{P_\ell} = K\frac{\tan(\chi_\phi) + \sin(\chi)\frac{P_y^{FPP}}{P_x^{FPP}}}{1 - \tan(\chi_\phi)\sin(\chi)\frac{P_y^{FPP}}{P_x^{FPP}}}$$

$$R = -K\frac{P_t}{P_\ell} \approx K\left[\chi_\phi + \sin(\chi)\frac{P_y^{FPP}}{P_x^{FPP}}\right],$$

$$K \equiv \mu_p\sqrt{\frac{\tau(1+\epsilon)}{2\epsilon}}$$

- FF ratio is highly sensitive to HMS non-dispersive bend angle at high Q^2
- At 8.5 GeV^2, $\frac{dR}{d\phi_{bend}} = -\frac{0.1}{mrad}$

$y_0^{fp} \pm \Delta y_0^{fp}$ (mm)	0 ± 10	0 ± 2
$\phi_0^{fp} \pm \Delta\phi_0^{fp}$ (mrad)	-0.05 ± 0.18	-0.03 ± 0.07
$y_0^{tar} \pm \Delta y_0^{tar}$ (mm)	-0.3 ± 0.2	-0.3 ± 0.1
$s_1 \pm \Delta s_1$ (mm)	0.8 ± 0.3	0.7 ± 0.1
$s_2 \pm \Delta s_2$ (mm)	1.0 ± 0.7	1.1 ± 0.2
$s_3 \pm \Delta s_3$ (mm)	2.7 ± 1.3	3.1 ± 0.8
$\phi^{(s)}_{bend} \pm \Delta\phi^{(s)}_{bend}$ (mrad)	0.16 ± 0.18	0.13 ± 0.07
$\phi^{(total)}_{bend} \pm \Delta\phi^{(total)}_{bend}$ (mrad)	0.12 ± 0.14	0.13 ± 0.08
χ^2/ndf	22.2/21	35.1/21

HMS Spin Transport Systematics—dispersive plane

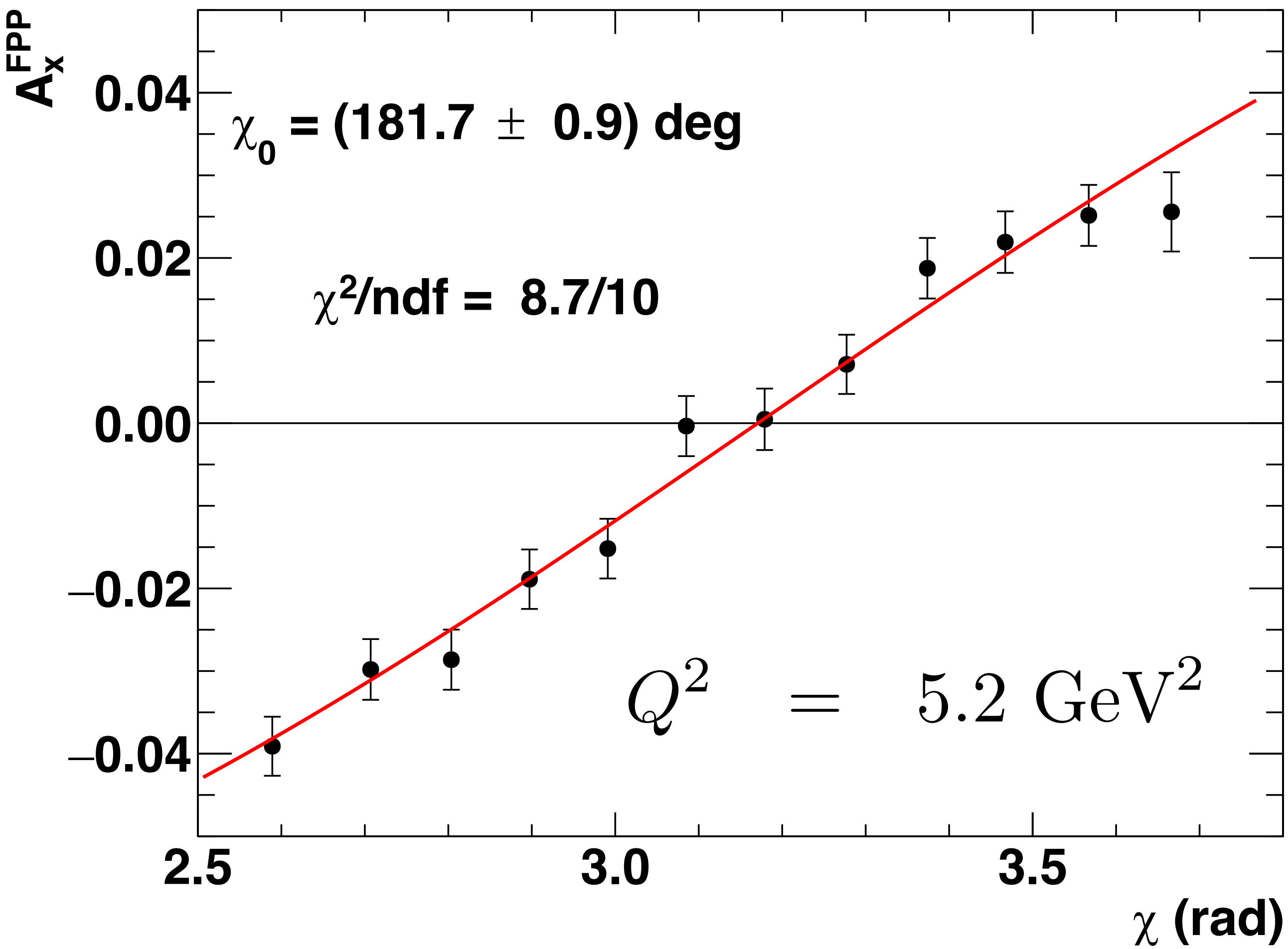

$$\text{Expected } \chi_0 = (180.42 \pm 0.02)^\circ$$
$$\text{Measured } \chi_0 = (181.7 \pm 0.9)^\circ$$
$$\Delta\theta_{bend} \approx \frac{\Delta\chi_0}{\gamma\kappa_p} = 3.2 \text{ mrad}$$

- Systematic uncertainty in dispersive-plane total bend angle estimated from asymmetry zero crossing at 5.2 GeV^2

Final Systematic Uncertainties—Ratio R

Table 3: Systematic uncertainty contributions for $R = -K\frac{P_t}{P_\ell} = \mu_p\frac{G_E^p}{G_M^p}$. The total systematic uncertainty includes the effects of partial correlations among the various systematic contributions, including $\Delta\phi_{tar}$ and Δy_{tar} (correlation coefficient $\rho_{\Delta\phi\Delta y} \approx -0.43$), and $\Delta\theta_{tar}$ and $\Delta\delta$ (correlation coefficient $\rho_{\Delta\theta\Delta\delta} \approx +0.26$). ΔR_{syst}^{total} is the total systematic uncertainty, while ΔR_{syst}^{ptp} is the "point-to-point" systematic uncertainty for $Q^2 = 2.5$ GeV^2 *relative* to the $\epsilon = 0.79$ setting.

Nominal Q^2 (GeV^2)	2.5	2.5	2.5	5.2	6.8	8.5
$\langle\epsilon\rangle$	0.153	0.638	0.790	0.38	0.52	0.24
$\frac{dR}{d\phi_{tar}}\Delta\phi_{tar}$	-3.4×10^{-3}	-2.1×10^{-3}	-2.0×10^{-3}	-4.8×10^{-3}	-5.7×10^{-3}	-0.010
$\frac{dR}{dy_{tar}}\Delta y_{tar}$	-2.0×10^{-3}	-1.2×10^{-3}	-1.2×10^{-3}	-2.9×10^{-3}	-3.9×10^{-3}	-7.7×10^{-3}
$\frac{dR}{d\theta_{tar}}\Delta\theta_{tar}$	-2.2×10^{-3}	-2.5×10^{-3}	-2.5×10^{-3}	1.4×10^{-3}	-5.0×10^{-3}	3.0×10^{-3}
$\frac{dR}{d\delta}\Delta\delta$	5.8×10^{-3}	1.2×10^{-3}	9.0×10^{-4}	1.2×10^{-3}	-3.3×10^{-6}	2.5×10^{-4}
$\frac{dR}{d\varphi_{FPP}}\Delta\varphi_{FPP}$	4.1×10^{-3}	2.5×10^{-3}	2.4×10^{-3}	4.6×10^{-4}	-6.0×10^{-3}	-0.017
$\frac{dR}{dE_e}\Delta E_e$	-1.8×10^{-3}	-1.1×10^{-4}	-5.6×10^{-5}	-1.9×10^{-4}	-8.3×10^{-5}	-1.4×10^{-4}
ΔR_{syst}(background)	3.5×10^{-4}	9.6×10^{-5}	9.9×10^{-5}	2.4×10^{-3}	1.6×10^{-3}	0.012
ΔR_{syst}^{total}	7.9×10^{-3}	4.0×10^{-3}	3.9×10^{-3}	5.5×10^{-3}	9.7×10^{-3}	0.024
ΔR_{syst}^{ptp}	4.3×10^{-3}	2.3×10^{-4}	1.1×10^{-4}	N/A	N/A	N/A

- Final systematic uncertainties for the FF ratio are somewhat reduced relative to the original (PRL) publications, owing largely to the more careful/thorough analysis of the non-dispersive-plane optics of the HMS, reducing the uncertainty of the total bend angle $\phi_{bend} = \phi_{fp} - \phi_{tar}$ to $\Delta\phi_{bend} = \pm0.14$ mrad.
- Partial correlations between uncertainties in $\Delta\phi_{tar}, \Delta y_{tar}$ and $\Delta\theta_{tar}, \Delta\delta$ are now accounted for in the final systematics.
- Most systematic contributions for R are strongly correlated between the three ϵ values at 2.5 GeV^2. Same HMS momentum setting implies same spin transport, FPP analyzing power, scattering angle reconstruction systematics, etc.

Final Systematic Uncertainties--P_ℓ/P_ℓ^{Born}

Table 4: Systematic uncertainty contributions for P_ℓ and the ratio P_ℓ/P_ℓ^{Born} at $Q^2 = 2.5$ GeV^2. The point-to-point systematic uncertainty is calculated *relative* to the $\langle\epsilon\rangle = 0.153$ setting. The total systematic uncertainties in P_ℓ do not include the global uncertainty of $\Delta P_e \approx 1\%$ in the beam polarization measurement. This is because any global overestimation (underestimation) of P_e is exactly compensated by an equal and opposite underestimation (overestimation) of the polarimeter analyzing power A_y. See text for details.

Q^2 (GeV^2)	2.5	2.5	2.5
$\langle\epsilon\rangle$	0.153	0.638	0.790
$\frac{dP_\ell}{d\phi_{bend}}\Delta\phi_{bend}$	1.3×10^{-4}	1.6×10^{-4}	1.3×10^{-4}
$\frac{dP_\ell}{d\theta_{bend}}\Delta\theta_{bend}$	4.2×10^{-3}	3.2×10^{-3}	2.5×10^{-3}
$\frac{dP_\ell}{dy_{tar}}\Delta y_{tar}$	8×10^{-5}	9×10^{-5}	8×10^{-5}
$\frac{dP_\ell}{d\delta}\Delta\delta$	-2.5×10^{-4}	-1.8×10^{-4}	-1.4×10^{-4}
$\frac{dP_\ell}{d\varphi_{FPP}}\Delta\varphi_{FPP}$	-1.6×10^{-4}	-2.0×10^{-4}	-1.7×10^{-4}
ΔP_ℓ (background)	8×10^{-5}	3×10^{-5}	2×10^{-5}
$\frac{dP_\ell}{dA_y}\Delta A_y$	N/A	-1.5×10^{-3}	-1.2×10^{-3}
$\frac{dP_\ell}{dP_e}\Delta P_e$	N/A	-3.7×10^{-3}	-2.9×10^{-3}
Total ΔP_ℓ^{syst}	4.2×10^{-3}	5.1×10^{-3}	4.0×10^{-3}
Total $\Delta_{syst}\left(\frac{P_\ell}{P_\ell^{Born}}\right)$	N/A	7.0×10^{-3}	7.1×10^{-3}
$\Delta_{syst}^{ptp}\left(\frac{P_\ell}{P_\ell^{Born}}\right)$	N/A	5.3×10^{-3}	6.1×10^{-3}

Summary and Conclusions

- Final GEp-III/GEp-2γ results published in archival Phys. Rev. C paper: A. J. R. Puckett *et al.*, Phys. Rev. C 96, 055203 (2017)
  - Come to JLab seminar this Friday, Jan. 26, CC auditorium, for full overview of experiment, final results, physics implications, and outlook for the future
- Technical details presented here are discussed in arXiv:1707.07750
- NIM article based on the above is forthcoming

Backup Slides

HMS Optics—x_{tar}/Raster Correction

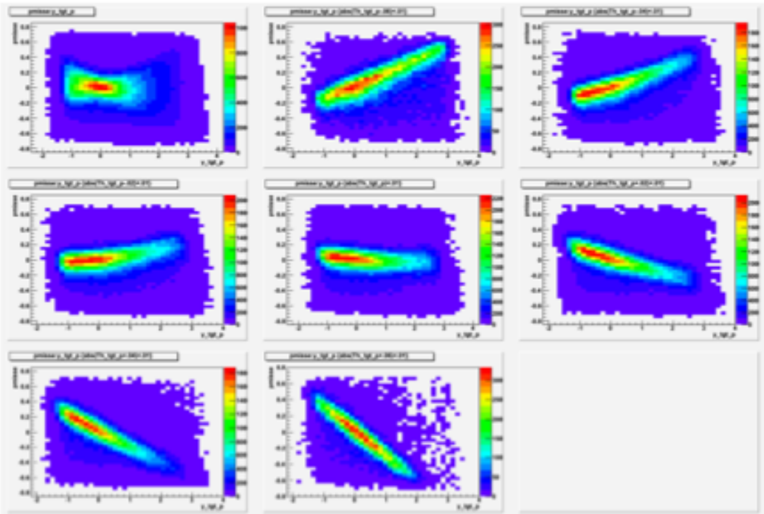

δp_e vs. y_{tar} for different θ_{tar} bins, no x_{tar} corrections

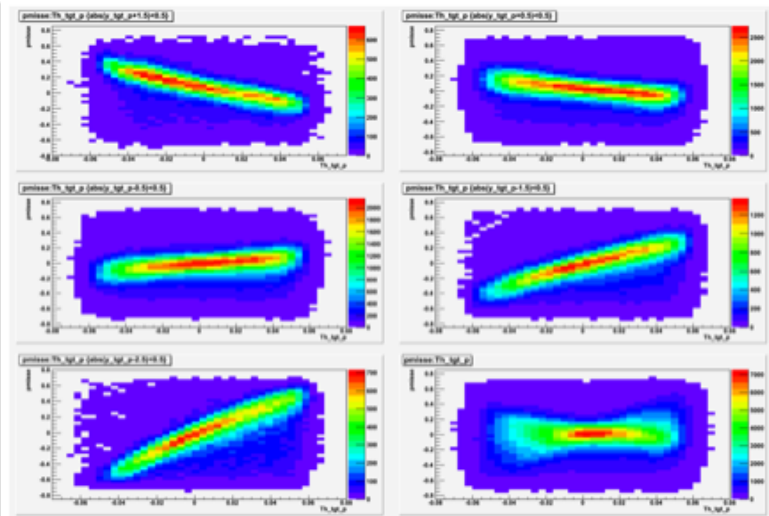

δp_e vs. θ_{tar} for different y_{tar} bins, no x_{tar} corrections.

The correction for x_{tar}, the vertical intersection of the trajectory with the plane perpendicular to the HMS optical axis containing the origin, is more important than usual for GEp-III due to long (20-cm) target.

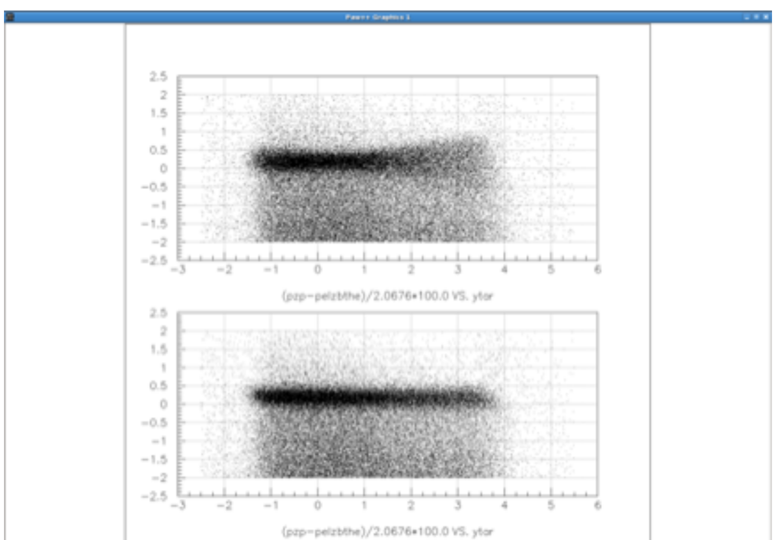

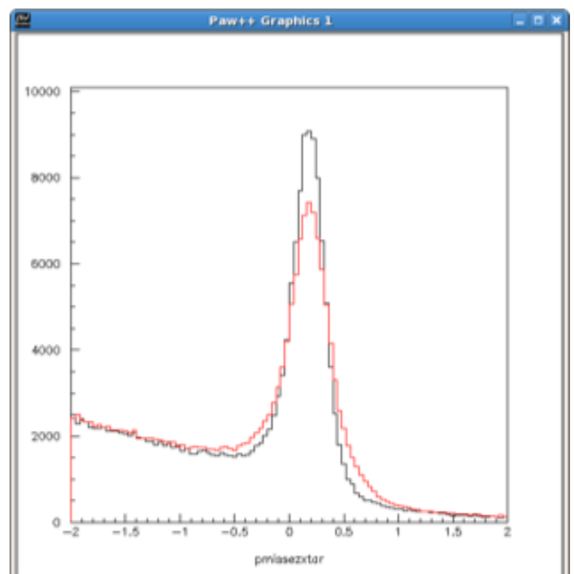

$$\delta p_p \equiv 100 \times \frac{p_p - p_p(\theta_p)}{p_0}$$

$$\delta p_e \equiv 100 \times \frac{p_p - p_p(\theta_e)}{p_0}$$

$$\delta\phi \equiv \phi_e - \phi_p - \pi$$

Improves resolution of elastic peak without changing the background shape→increases signal/background ratio

Variable-Width Exclusivity Cuts (GEp-2γ)

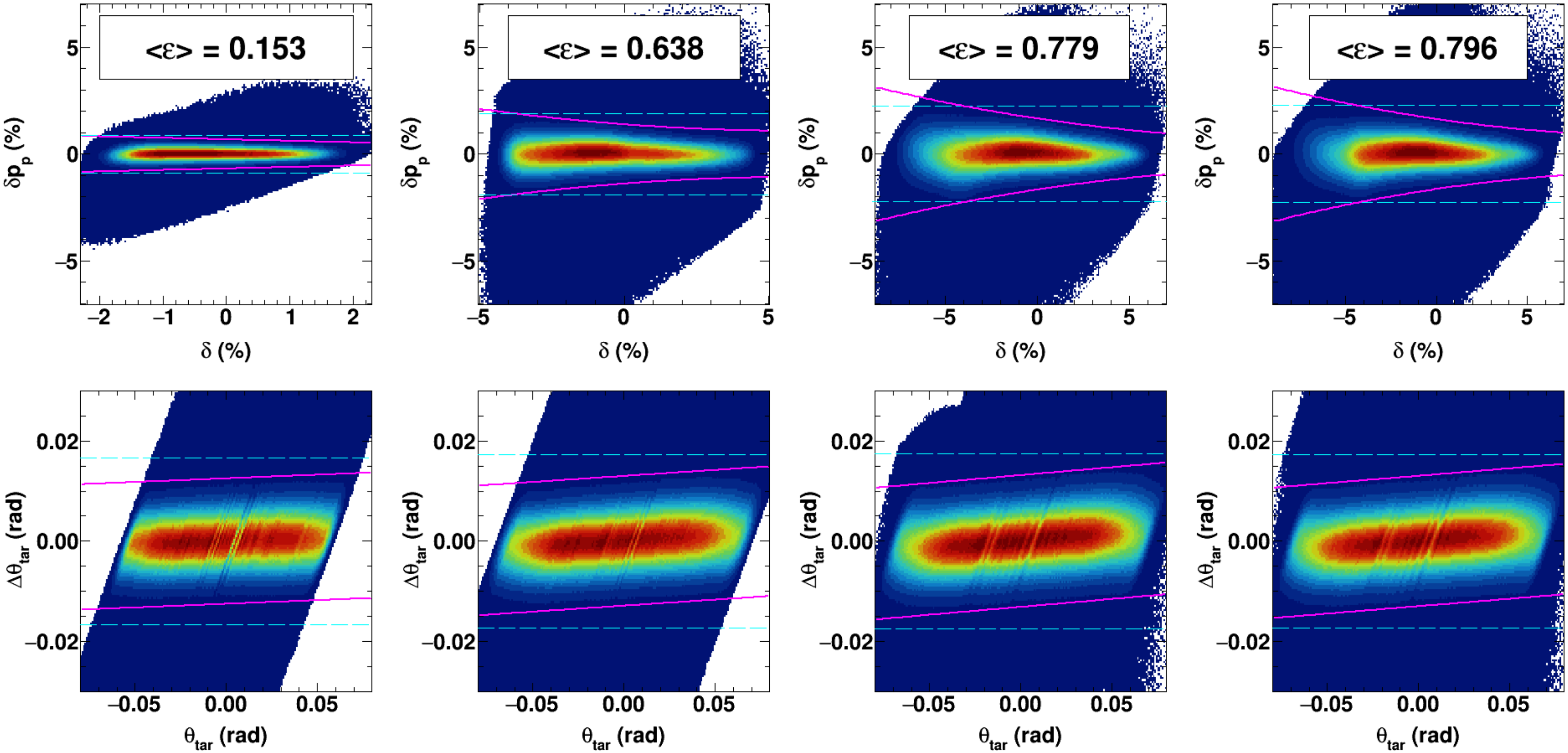

- Resolution of $\delta p_p \equiv 100 \times (p_p - p_p(\theta_p))/p_0$ varies by more than a factor of two as a function of δ within the HMS acceptance for highest ϵ.
- $\Delta\theta_{tar} \equiv \theta_{tar} - \theta_{tar}(\phi_e, \theta_e)$ exhibits slight correlation with θ_{tar}. Deviation from zero does not exceed 2 mrad anywhere in the acceptance.

Variable-width exclusivity cuts (GEp-III)

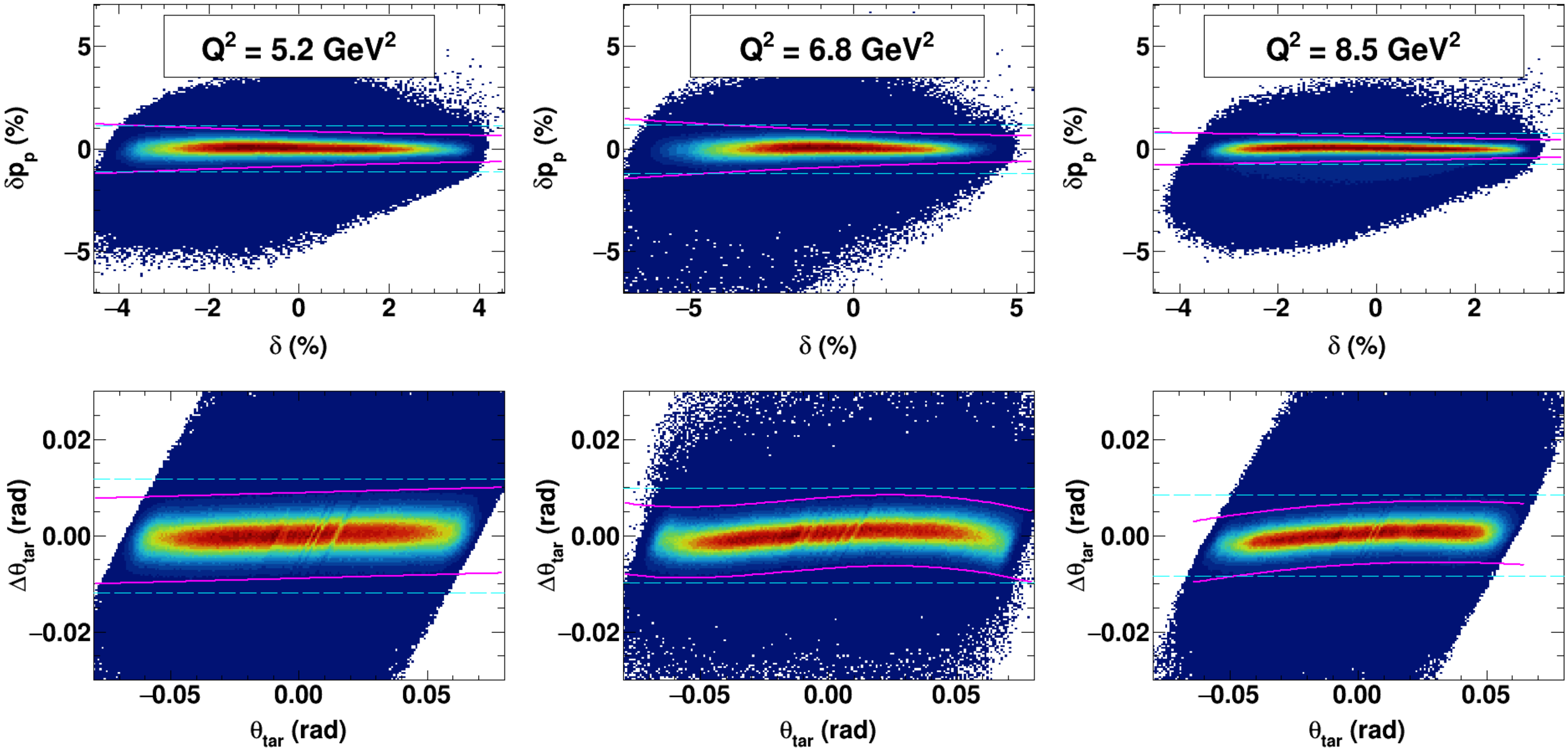

- $\Delta\theta_{tar}$ vs. θ_{tar} correlation exhibits some small non-linearity for $Q^2 = 6.8, 8.5$ GeV². These non-linear distortions are attributable to a +3 mm vertical beam position offset during these kinematics; the x_{tar}-dependent matrix elements are not independently calibrated and are fixed during the calibration of x'_{tar}, which took place with the beam vertically centered.

All exclusivity cuts vs. proton kinematics, 8.5 GeV^2

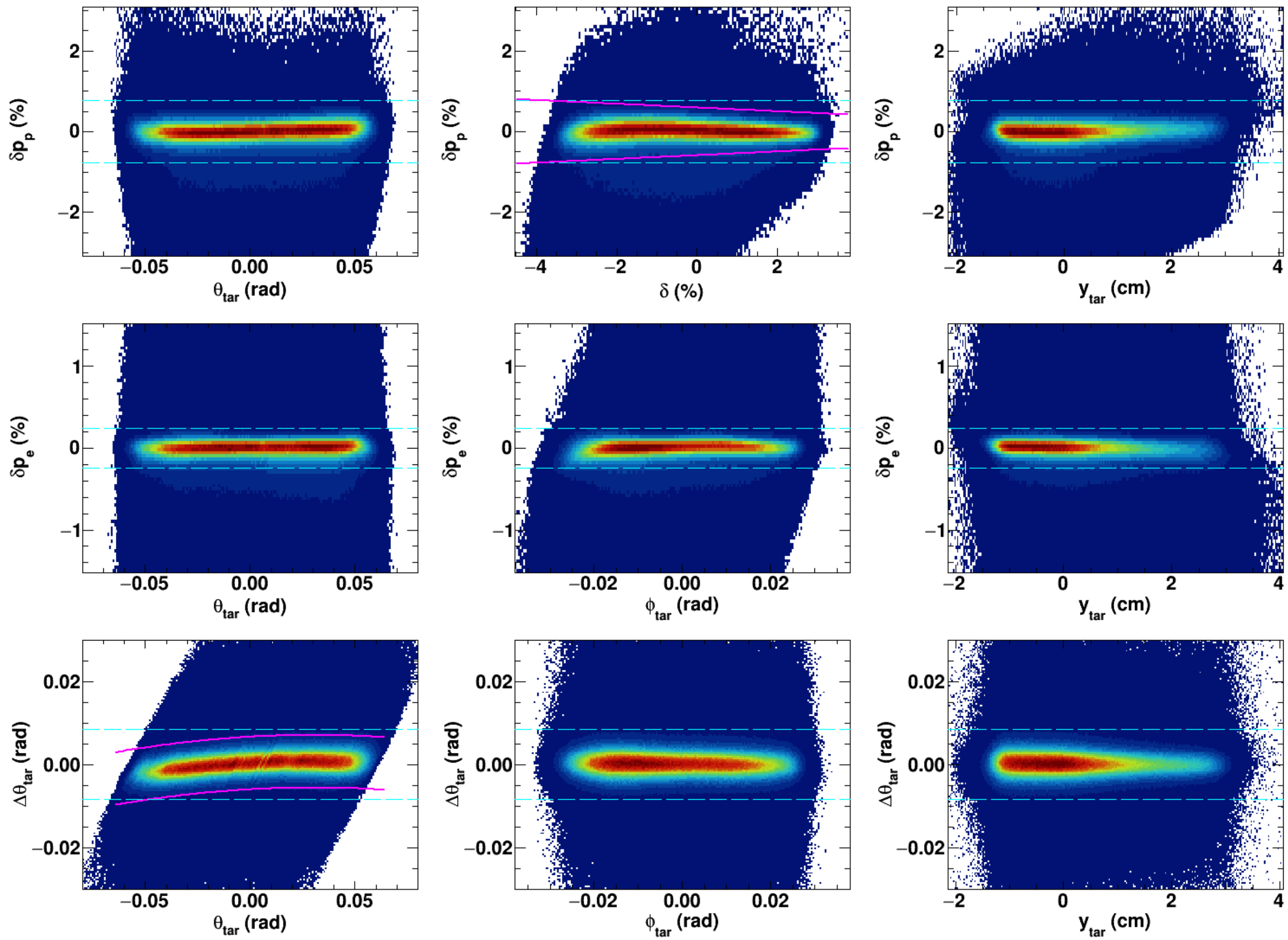

$$\delta p_p \equiv 100 \times \frac{p_p - p_p(\theta_p)}{p_0}$$

$$\delta p_e \equiv 100 \times \frac{p_p - p_p(\theta_e)}{p_0}$$

$$\delta \phi \equiv \phi_e - \phi_p - \pi$$

- δp_e resolution is roughly independent of proton kinematics within the acceptance, and is dominated by HMS momentum resolution → $\pm 3\sigma$, fixed-width cuts used.
- $\delta p_e, \delta \phi$ are dominated by HMS angular resolutions, use variable-width cuts to optimize efficiency, signal-background ratio, and avoid cut-induced bias of spin transport calculation